Journal Pre-proof

Accelerated computational micromechanics and its application to polydomain liquid crystal elastomers

Hao Zhou, Kaushik Bhattacharya

PII: S0022-5096(21)00143-5
DOI: https://doi.org/10.1016/j.jmps.2021.104470
Reference: MPS 104470

To appear in: *Journal of the Mechanics and Physics of Solids*

Received date : 18 February 2021
Revised date : 21 April 2021
Accepted date : 22 April 2021

Please cite this article as: H. Zhou and K. Bhattacharya, Accelerated computational micromechanics and its application to polydomain liquid crystal elastomers. *Journal of the Mechanics and Physics of Solids* (2021), doi: https://doi.org/10.1016/j.jmps.2021.104470.

Accelerated computational micromechanics and its application to polydomain liquid crystal elastomers

Hao Zhou & Kaushik Bhattacharya

Division of Engineering and Applied Science
California Institute of Technology
Pasadena CA 91125

Abstract

We present an approach to solving problems in computational micromechanics that is amenable to massively parallel calculations through the use of graphical processing units (GPUs) and other accelerators. We apply it to study microstructure evolution in polydomain liquid crystal elastomers (LCEs). LCEs are rubber-like solids where rod-like nematic molecules are incorporated into the main or a side polymer chain. They undergo isotropic to nematic phase transition accompanied by spontaneous deformation which can be exploited for actuation. Further, they display a soft behavior at low temperatures due to the reorientation of the nematic directors. The problem of understanding nematic reorientation in the presence of realistic defects (non-ideality) is computationally expensive, and we address this by efficiently exploiting GPUs. The approach is broadly applicable to various phenomena including crystal plasticity and phase transitions that are described by internal variable theories. We verify the approach against previous calculations and establish its performance by studying long wavelength instability of finite elasticity. Our numerical studies of LCEs provides insights into the director distribution and reorientation in polydomain specimens, and how these lead to soft behavior under multiaxial loading. The results show good agreement with experimental observations.

1 Introduction

Liquid crystal elastomers (LCEs) are synthetic materials made by incorporating rod-like nematic mesogens into the polymer chains of an elastomer [63]. The combination of polymer elasticity and nematic ordering gives rise to exotic mechanical behavior. At high temperatures, the mesogens are randomly oriented and the LCE is an isotropic rubbery solid. However, on cooling, they undergo a phase transition where the steric interactions between the mesogens cause them to align in a particular direction. The isotropic to nematic phase transition is accompanied by a spontaneous deformation. Thus, they have been proposed

for applications as actuators and for shape-morphing. Further, below the transition temperature, the nematic director can reorient resulting in a soft behavior [33]. We refer the reader to Warner and Terentjev [63] for a comprehensive introduction.

Our focus is LCEs that are synthesized in the isotropic phase and then cooled. There is typically some small non-uniformity of cross-linking during synthesis, and this leads to a local preference for the nematic orientation that is not uniform ('random'). This results in a *polydomain* state where the nematic director is highly non-uniform. The application of stress can reorient the director, but there is an energetic cost [12]. This leads to semi-soft behavior in such isotropic-genesis polydomain materials [59], and this is attractive for a number of damping applications. Indeed, the viscoelastic response of such materials has also been a subject of recent interest [5]. Finally, recent experiments have shown rather unusual behavior in biaxial loading where unequal stretch leads to equal true stress [55]. The *first goal* of this paper is to study the underlying mechanism of microstructure evolution in isotropic-genesis polydomain materials subjected to multiaxial stress.

We start with a continuum model that treats the director as an internal variable, has a free energy density that includes contributions from the entropy of the polymer chains [14], the energetic cost of reorientation [12], nematic or Frank elasticity that penalizes gradients in the director [63], and dissipation that accounts for director reorientation and viscosity. The 'ideal' model, where the typically small reorientation and Frank contributions are neglected, has been widely studied in the static setting. This theory is not convex and leads to stripe domains and other fine-scale microstructure leading to soft behavior [63]. Indeed, DeSimone and Dolzmann [19] explicitly calculated the relaxed energy or the effective energy that implicitly accounts for the microstructure in this ideal situation, and this energy has been the basis of macroscopic finite element simulations [18, 51]. There are also some detailed study of microstructure evolution [38, 66], but they focus on monodomain specimens. In polydomain specimens, Biggins *et al.* [13, 11] used bounds to establish the semi-soft behavior in uniaxial tension while Uchida [57, 58] studied semi-soft behavior with a related model based on random networks. The focus of this work is microstructure evolution in polydomain materials, and its macroscopic consequence under multiaxial loading.

This naturally leads to a problem of computational micromechanics where we conduct detailed numerical simulation of microstructure evolution using periodic boundary conditions on a domain that is a representative of the macroscopic material. Similar problems been widely studied in a number of phenomena including elasticity, crystal plasticity and phase transformations [68]. In all these situations, the state of the solid is described by the deformation gradient and a (set of) internal variables, which evolve to satisfy mechanical equilibrium and kinetic relations subject to initial and boundary conditions. These lead to nonlinear partial differential equations that are second order in space and first order in time, and the solution to such problems can be computationally demanding especially since they have to be performed repeatedly for various initial and boundary conditions to understand the overall behavior.

A recent trend in computing platforms is to complement the central processing units (CPUs) with massively parallel accelerators like graphical processing units (GPUs) [30, 32]. Such accelerators contain thousands of processors, but these are not independent. Instead, they are grouped together in 'warps' that share a memory and execute the same instructions but on possible different data (SIMD). Consequently, they can provide enormous computa-

tional power if the calculations are carefully arranged to meet the limitations of the architecture. The *second goal* of this work is to exploit such accelerators in the solution of problems in micromechanics.

To do so, we observe that the nonlinear partial differential equations that describe the phenomena of interest come about through a *composition* of kinematic compatibility, balance laws (mass, momenta, energy) and material behavior. The compatibility and balance laws are nonlocal, but may be interpreted as projections in appropriate function space. The material behavior is nonlinear and may involve time derivatives, but is spatially *local*. Each of these can be implemented on accelerators, and the challenge is to solve their composition. We start from a (incremental) variational principle, formulate the kinematic compatibility as a constraint using an augmented Lagrangian, and then use the alternating direction method of multipliers (ADMM). Our approach leads to a special case of the augmented Lagrangian approach of Michel, Moulinec and Suquet [39].

In their pioneering work, Moulinec and Suquet [47] recognized that the periodic boundary conditions that are of interest in computational micromechanics make it natural to use the fast Fourier transform (FFT) in its solution. They rewrite the problem of equilibrium in a heterogeneous linear elastic medium to a Lippmann-Schwinger type equation which they solve iteratively using FFT. Since then FFT-based methods have been widely used in a variety of applications (e.g.thermoelasticity [2], elasto-viscoplasticity [36], dislocations [7], piezoelectric materials [61], shape-memory polycrystals [10], and crack prediction of brittle materials [54]). The method has been understood as a Neumann series approximation [45, 43]. Various approaches to accelerate the convergence have been introduced[22, 39, 45, 43]. We refer the reader to Moulinec and Silva [46] and Moulinec, Suquet and Milton [48] for a discussion. More recently, the Fourier-Galerkin method of Vondřejc, Zeman and Marek [62] has gained in popularity. It formulates the governing equations using a variational approach, uses a Fourier basis for approximation and performs well compared to other FFT-based methods [44].

The computational implementation of these methods have largely focussed on CPUs, though there is recent work on the use of GPUs. Bertin and Capolungo [8] used GPUs for the FFT while other researchers have used GPUs for the constitutive update [42, 31, 21]. However, these works limit the use of GPUs to particular aspects of the overall algorithms. Our approach exploits the parallel efficiency of GPUs for the entire algorithm.

We present our computational approach in Section 2, and the implementation in GPUs in Section 3. While the current work is motivated by LCEs, the formulation is presented in a general way. We verify our framework by the study of the long wavelength instability of finite elasticity in Section 4. The results are compared with previous numerical simulations. The example also shows how stability analysis with Bloch waves can easily be incorporated into the approach. We also use this example to study convergence and parallel performance. We turn to LCEs in Section 5. We present the formulation, study stripe domains in monodomain specimens and then turn study microstructure evolution under uniaxial and biaxial loading in polydomain LCEs. We conclude in Section 6 with a discussion of open issues.

2 Method

2.1 Formulation

It is common in a number of phenomena in solids including plasticity (e.g. [53]), phase transitions (e.g. [3]) and fracture (e.g. [15]) to describe the state of the solid by a deformation gradient F and a set of internal variables η (phase fraction, plastic activity, director field, fracture field etc.). In the absence of inertia, these are governed by a pair of coupled nonlinear partial differential equations:

$$\nabla \cdot (W_F(\nabla u, \eta, x)) = 0, \tag{1}$$
$$W_\eta(\nabla u, \eta, x) + D_v(\eta_t, x) = 0 \tag{2}$$

where $u : \Omega \times [0,T] \to \mathbb{R}^3$ is the deformation, $F : \Omega \times [0,T] \to \mathbb{R}^{3\times 3}$ is the deformation gradient, $\eta : \Omega \times [0,T] \to \mathbb{R}^d$ is an internal variable or order parameter, $v = \eta_t$ is the rate of change of the internal variable, $W : \mathbb{R}^{3\times 3} \times \mathbb{R}^d \times \Omega \to \mathbb{R}$ is the stored (elastic) energy density, $D : \mathbb{R}^d \times \Omega \to \mathbb{R}$ is the dissipation potential (rate of dissipation as a function of the rate of change of internal variable) that governs the evolution of the internal variables, $\Omega \subset \mathbb{R}^3$ is the reference domain assumed to be simply connected, T is the final time of interest and the subscripts denote partial differentiation. Here and in what follows all operators and identities are defined on the reference configuration. The first of the two equations describes the mechanical equilibrium, and the second describes the kinetic relation or configurational equilibrium that governs the evolution of the internal variables (we refer the reader to [50, 40] for details of rewriting the kinetic relation in this gradient-flow form).

The first equation above is a second-order nonlinear elliptic partial differential equation in space with time as a parameter. The second is typically first order in time with space as a parameter, and also nonlinear. Further, in rate independent phenomena, the dissipation potential may not be continuously differentiable and the second equation is interpreted as a differential inclusion [40]. These make the system (1,2) challenging to solve. In particular, traditional finite-element approaches require significant amounts of communication to solve in parallel.

However, these equations arise from the agglomeration of a number of simpler equations:

$$\text{Compatibility:} \qquad F = \nabla u \iff \operatorname{curl} F = 0, \tag{3}$$
$$\text{Equilibrium:} \qquad \nabla \cdot S = 0, \tag{4}$$
$$\text{Stress-Strain Relation:} \qquad S = W_F(F, \eta, x), \tag{5}$$
$$\text{Kinetic relation:} \qquad W_\eta(F, \eta, x) + D_v(\eta_t, x) = 0. \tag{6}$$

Note that the field equations – the first two – are linear and universal, while the constitutive updates – the last two – are local (albeit nonlinear). We want to exploit this in the GPU implementation.

In order to do so, consider an implicit time discretization

$$\text{Compatibility:} \qquad F^{n+1} = \nabla u^{n+1} \iff \text{curl } F^{n+1} = 0, \tag{7}$$

$$\text{Equilibrium:} \qquad \nabla \cdot S^{n+1} = 0, \tag{8}$$

$$\text{Stress-Strain Relation:} \qquad S^{n+1} = W_F(F^{n+1}, \eta^{n+1}, x), \tag{9}$$

$$\text{Kinetic relation:} \qquad W_\eta(F^{n+1}, \eta^{n+1}, x) + D_v\left(\frac{\eta^{n+1} - \eta^n}{\Delta t}, x\right) = 0. \tag{10}$$

This can be written as the following variational problem (e.g., [50]):

$$u^{n+1}, \eta^{n+1} = \arg\min \int_\Omega \left(W(\nabla u, \eta, x) + \Delta t D\left(\frac{\eta - \eta^n}{\Delta t}, x\right)\right) dx \tag{11}$$

or as the following constrained variational problem

$$F^{n+1}, \eta^{n+1} = \underset{\text{curl F}=0}{\arg\min} \int_\Omega \left(W(F, \eta, x) + \Delta t D\left(\frac{\eta - \eta^n}{\Delta t}, x\right)\right) dx. \tag{12}$$

We rewrite this constrained variational problems using the *augmented Lagrangian* method or method of multipliers (e.g. [24]). Given $\rho > 0$, we seek to find the saddle point:

$$\int_\Omega \left(W(F, \eta, x) + \Delta t D\left(\frac{\eta - \eta^n}{\Delta t}, x\right) + \Lambda \cdot (\nabla u - F) + \frac{\rho}{2}|\nabla u - F|^2 \right) dx \tag{13}$$

for u, F and the Lagrange multiplier $\Lambda : \Omega \to \mathbb{R}^{3\times 3}$. We solve this problem using the *alternating direction method of multipliers (ADMM)* [24, 25, 28] which is an iterative method.

At the $(n+1)^{th}$ time step, given $F^n, \eta^n, u^n, \Lambda^n$, set $F_0 = F^n, \eta_0 = \eta^n, u_0 = u^n, \Lambda_0 = \Lambda^n$ and iterate over i

- *Step 1: Local problem.* Update F, η by solving at each x

$$W_F(F_{i+1}, \eta_{i+1}, x) - \Lambda_i - \rho(\nabla u_i - F_{i+1}) = 0, \tag{14}$$

$$W_\eta(F_{i+1}, \eta_{i+1}, x) + D_v\left(\frac{\eta_{i+1} - \eta^n}{\Delta t}, x\right) = 0. \tag{15}$$

- *Step 2: Helmholtz projection.* Update u by solving the partial differential equation

$$-\Delta u_{i+1} = \nabla \cdot \left(-F_{i+1} + \frac{1}{\rho}\Lambda_i \right). \tag{16}$$

- *Step 3: Update Lagrange multiplier.* Update Λ as

$$\Lambda_{i+1} = \Lambda_i + \rho(\nabla u_{i+1} - F_{i+1}). \tag{17}$$

- *Step 4: Check for convergence.* Check both primal and dual feasibility:

$$r_p := ||\nabla u_{i+1} - F_{i+1}||_{L^2} \le r_p^{\text{tolerance}}, \quad r_d := \rho/\mu ||\nabla u_{i+1} - \nabla u_i||_{L^2} \le r_d^{\text{tolerance}} \tag{18}$$

for given $r_p^{\text{tolerance}}, r_d^{\text{tolerance}}$ and representative elastic modulus μ.

until convergence and update $F^{n+1} = F_i, \eta^{n+1} = \eta_i, u^{n+1} = u_i, \Lambda^{n+1} = \Lambda_i$.

We now make a series of comments about the proposed approach.

Augmented-Lagrangian method. As already noted in the introduction, the approach above is a special case of the Augmented-Lagrangian method of Michel, Moulinec and Suquet [39]. In our language, they study the functional

$$\int_\Omega \left(W(F,\eta,x) + \Delta t D\left(\frac{\eta-\eta^n}{\Delta t}, x\right) + \Lambda\cdot(\nabla u - F) + \frac{\rho}{2}(\nabla u - F)\cdot\mathbb{C}_0(\nabla u - F)\right) dx \quad (19)$$

where $\rho\mathbb{C}_0$ is the modulus of a comparison medium. They study convergence with ρ at low spatial resolution and use this value at high spatial resolution. Our approach is a special case of their method with $\mathbb{C}_0 = \mathrm{Id}$. The advantage of doing so is that it leads to a Helmholtz projection in Step 2 as opposed to an operator that depends on the comparison medium. Further, we tune ρ during iteration (cf. (20)) and explore the approximate solution of the local problem. This algorithm was also used in for finite elasticity (no internal variables) in the context of general boundary value problems and finite elements by Glowinski and Le Tallec [26, 27].

We comment that we could have chosen a different constant ρ' instead of ρ in equation (17) that updates the Lagrange multiplier (Step 3). An analysis of Eckstein and Bertsekas [20] suggests that using $\rho' > \rho$ may improve convergence. We have not explored this in our work. We also note that the original formulation of Michel, Moulinec and Suquet [39] used a modulus $\mathbb{D}_0$ distinct from the comparison medium $\mathbb{C}_0$ in this step, though the common implementations use $\mathbb{C}_0 = \mathbb{D}_0$.

Parallel implementation. Step 1 is local, and can be solved trivially in parallel. However, it is (generally) nonlinear and therefore requires an iterative approach. In this work, we solve it using a steepest descent method with backtracking line search. A potential difficulty is that different spatial points may require different number of iterations to converge, and we address it below. Step 2 leads to a universal Poisson's equation for which there are a number of effective parallel solvers. In this work, we consider problems with periodic boundary conditions and therefore use the fast Fourier transform. Step 3 is a trivial local update, and step 4 a simple check. Thus, this iterative algorithm can be implemented effectively using accelerators like Graphical Processing Units (GPUs) as we demonstrate in the subsequent sections.

Convergence. Boyd *et al.* [16] prove the convergence of the spatially discretized version of the algorithm for ρ large enough under the hypotheses that W is convex and the unaugmented functional with $\rho = 0$ has a saddle point. They also review improvements of this result in the literature. However, it is not natural to expect W to be convex in F in finite deformation. Here, there are results in the case of elasticity where there is no internal variable. Glowinski and Le Tallec [26] show that the weak form of equilibrium equation of incompressible elasticity is equivalent to the weak form of the first variation of the augmented Lagrangian functional. Further, Glowinski and Le Tallec [27] show in the case of Mooney-Rivlin materials that the finite element discretization of this iterative approach converges for sufficiently large ρ. Furthermore, they show that the finite element solutions converge to the solution of the continuous problem. Their arguments can be generalized to a larger class of incompressible, isotropic, polyconvex, hyperelastic materials [28]. However, the general case with internal variables remains open.

Connection to physics. This iterative method also has a close connection to the physics as the various steps and convergence criteria can be identified with the governing equations (3) through (6). Indeed, we can see that (15) is a time-discretized version of the kinetic relation (6). As the method converges, the primal convergence $(18)_1$ guarantees that $F \approx \nabla u$ or satisfaction of the compatibility equation (3). We now turn to the stress-strain relation (5). As a result of the the primal convergence, we observe that (14) becomes $W_F \approx \Lambda$. This tells us that the Lagrange multiplier converges to the stress and (14) approximates the stress-strain relation (5). Finally, we show in the appendix that the dual convergence is equivalent to the equilibrium condition (4).

Penalty parameter. We have noted above that the method is known to converge under suitable hypothesis on W, D for all ρ sufficiently large [16, 27]. However, the rate of convergence depends critically on the choice of ρ. We adapt an idea proposed by He, Yang and Wang [29] to adaptively change ρ with iteration guided by r_p and r_d. A large ρ better enforces compatibility (cf. 16) and leads to a faster drop of the primal error r_p. However, it leads to a poor enforcement of the constitutive equation (cf. 14) and slower drop of the dual error r_d. Conversely, a small ρ leads to a faster drop of the dual error r_d, but a slower drop of the primal error r_p. After checking for convergence, we adjust ρ as

$$\rho_{i+1} = \begin{cases} \gamma\rho_i, & \text{if} \quad r_p/r_d > \tau \\ \max\{\rho_i/\gamma, \rho_{\min}\}, & \text{if} \quad r_d/r_p > \tau \\ \rho_i, & \text{if} \quad else \end{cases} \tag{20}$$

for given γ, τ $\rho_{\min}$. We take γ and τ to be 1.3 and 10 respectively to avoid too frequent updates. $\rho_{\min}$ enforces the requirement that ρ remains large enough for the method to converge and the choice of $\rho_{\min}$ depends on W. An important observation is that this is enabled by the fact that the Laplace operator in (16) is independent of ρ. We report a numerical study in Section 4.2 and specifically in Figure 4.

Approximate solution of the local problem. While the local problem (14), (15) is trivially parallelizable, a potential problem is that different points may require a different number of iterations to converge to a given point-wise residual error. Indeed, in practice (as we shall see in Section 4.2), a few isolated points require a very large number of iterations to converge compared to the rest. Unfortunately, the calculation can not advance to the next step until the last point has converged, and consequently, these slowly-converging points can add significantly to the computational cost. However, Eckstein and Bertsekas [20] have proved that for convex W, the algorithm converges when the the local error is summable. In other words, it is not necessary to solve the local equations (14), (15) at every point (i.e., in L^∞ norm), but it suffices to solve them in some L^p norm for appropriate $2 \leq p < \infty$. Working in $p = 2$, set the local residual to be

$$r_l = \frac{1}{\mu}||W_F(F_{i+1}, \eta_{i+1}, x) - \Lambda^n + \rho(\nabla u_i - F_{i+1})||^2_{L^2}. \tag{21}$$

We see from (43) in the Appendix that equilibrium is still satisfied if the both the dual and local residual go to zero. Thus, satisfaction of the equilibrium equation does not require

pointwise convergence. Further savings can be achieved by keeping the local residual large in the initial (global) iterations, and gradually reducing it as (global) convergence is achieved [16]. We explore two strategies in Section 4.2. In one, we maintain a balance between r_l and r_d while in the other we require a fixed fraction of local points to converge.

While these approaches reduce the number of iterations of the local problem, computing either the local residual r_l or the fraction of converged points requires a communication between the various points which can be expensive in an accelerator. Therefore it is necessary to balance the cost of iteration and the cost of checking convergence. We study this balance in Section 4.2.

Gradient internal variables. In certain problems like phase transitions and microstructure evolution (like the one we shall study in Section 5), the state of the material is described not only by an internal variable, but also the gradient of the internal variable, i.e,. $W = W(F, \eta, \nabla\eta, x)$. These can be incorporated into the method in two ways.

The first approach is to treat the gradient of the internal variable in much the same way that we treat the deformation gradient. But this requires some care to maintain the linear structure of step 2. We introduce two internal variables, ℓ and H and enforce the constraints $\ell = \eta$, $H = \nabla\eta$ using the augmented Lagrangian, i.e., consider the Lagrangian density

$$\begin{aligned} &W(F, \ell, H, x) + \Delta t D + \Lambda \cdot (\nabla u - F) + \rho/2|\nabla u - F|^2 \\ &\quad + \mu \cdot (\nabla\eta - H) + \xi/2|\nabla\eta - H|^2 + \kappa \cdot (\ell - \eta) + \zeta/2|\ell - \eta|^2 \end{aligned}$$

with additional Lagrange multipliers μ, κ and penalty parameters ξ, ζ. We minimize the Lagrangian with respect to F, ℓ and H in step 1 and with respect to u and η in step 2. We then update all the Lagrange multipliers in step 3 and check convergence in step 4. Note that the equation in step 2 describing η is not the Poisson's equation but includes a linear term in η; still, it can be treated as before, similar to Section 2.3.

The second approach is to use the value of the gradient from the previous iteration. In other words, we rewrite (15) as

$$W_\eta(F_{i+1}, \eta_{i+1}, \nabla\eta_i, x) + D_v\left(\frac{\eta_{i+1} - \eta^n}{\Delta t}, x\right) = 0. \tag{22}$$

While this is approximate, it is effective. In most models, the gradient of the internal variable is introduced as a way of introducing a length scale, and this approximation does so effectively. We use this second approach in Section 5.

2.2 Implementation in the periodic setting

It is common in computational micromechanics to consider a material that is periodic and a representative volume element that is a unit cell. In other words, $\Omega = (-L, L)^3$ and $W(F, \eta, x), D(\eta_t, x)$ are periodic in x. Further, the average deformation gradient $\langle F\rangle$ is prescribed in strain-controlled simulations, the average stress $\langle S\rangle$ is prescribed in stress-controlled simulations and some combination with some components of $\langle F\rangle$ and complementary components of $\langle S\rangle$ are prescribed in mixed simulations (e.g., plane stress where the

average planar stretch is prescribed – see for example [37] for a comprehensive discussion of mixed boundary conditions). Above, $\langle\cdot\rangle$ denotes spatial average.

We assume that the resulting deformation gradient F, internal variable η and stress S are also periodic in x. This implies that the deformation u is periodic up to a linear function; i.e., $u-\langle F\rangle x$ is periodic. It is then natural to solve Step 2 (16) using fast Fourier transforms (FFT). In Fourier space, (16) becomes local (i.e., can be solved at each ξ) as

$$\hat{u}(\xi) = -\frac{(\hat{F}-\rho^{-1}\hat{\Lambda})i\xi}{|\xi|^2}. \tag{23}$$

where $\hat{f}(\xi)$ denotes the Fourier transform of $f(x)$ and i is the imaginary unit. Thus, we solve Steps 1, 3 and 4 in real space and Step 3 in Fourier space using FFT and iFFT (inverse fast Fourier transform) to go back and forth between them. Specifically, we consider a regular $N\times N\times N$ grid (for N even) on Ω in real space, and the corresponding $N\times N\times N$ on the domain $(-\frac{\pi}{L},\frac{\pi}{L})^3$ in Fourier space. We define $\hat{f}(\xi)$ as the discrete Fourier transform on this space and use FFT to evaluate it.

A couple of comments are in order. First, it is convenient to work with

$$\tilde{u} = u-\langle\nabla u\rangle x, \quad \tilde{F} = F-\langle F\rangle, \quad \tilde{\Lambda} = \Lambda-\langle\Lambda\rangle \tag{24}$$

which are all periodic (recall that u is not necessarily periodic). This is also convenient since the boundary conditions are prescribed in terms of $\langle F\rangle$ or $\langle S\rangle$ (recall Λ converges to S).

Second, the material may be heterogeneous and W, D may be discontinuous functions of x in many problems of interest. In such situations, F,η may be discontinuous and thus the use of Fourier transforms to solve for u may lead to spurious oscillations. An approach around this that has proved very effective in various problems[6, 35, 61] using the closely related Lippmann-Schwinger approach is to replace the discrete Fourier transform of the derivatives with the discrete Fourier transform of the central differences:

$$\widehat{u_{i,j}}(\xi) = i\hat{u}_i(\xi)\xi_j \quad \text{with} \quad \frac{\widehat{u_i(x+he_j)}-\widehat{u_i(x-he_j)}}{2h}(\xi) = i\hat{u}_i(\xi)\frac{\sin(h\xi_j)}{h}, \tag{25}$$

$$\widehat{u_{i,jj}}(\xi) = -\hat{u}_i(\xi)|\xi_j|^2 \quad \text{with} \quad \frac{\widehat{u_i(x+he_j)}+\widehat{u_i(x-he_j)}-2\widehat{u_i(x)}}{h^2}(\xi) = -\hat{u}_i(\xi)\frac{4\sin^2(\frac{h\xi_j}{2})}{h^2} \tag{26}$$

where $\widehat{u_i(x+he_j)}$ is the Fourier transform of $u_i(x+he_j)$ etc. Since $\sin\alpha/\alpha<1$, this is equivalent to a high frequency filter and suppresses the spurious oscillations. We refer the reader to [67] for further discussion.

2.3 Quadratic functionals and Bloch waves

We conclude this section with the discussion of a closely-related linear problem that arises in the study of stability of periodic solutions to nonlinear problems. Let $\mathbb{L}_{ijkl}(x)$ be a periodic fourth order tensor field of period 1 with $\mathbb{L}_{ijkl}=\mathbb{L}_{klij}$. We are interested in evaluating

$$\beta_k = \min_{v\in\mathrm{Re}\ \mathcal{A}_k}\int_{\Omega_0}\frac{1}{2}\overline{v}_{i,j}\mathbb{L}_{ijkl}v_{k,l}dx = \min_{v\in\mathrm{Re}\ \mathcal{A}_k}\int_{\Omega_0}\nabla\overline{v}\cdot\mathbb{L}\nabla v\ dx \tag{27}$$

over an admissible class of functions that are unit Bloch waves:

$$\mathcal{A}_k = \left\{ v \in H^1(\Omega_0) : ||v||_{L^2(\Omega_0)} = 1,\ v(x) = p(x)\exp(i\omega_k \cdot x),\ \omega_k = \left\{ \frac{2\pi}{k_1}, \frac{2\pi}{k_2} \right\},\ p\ 1-\text{periodic} \right\} \tag{28}$$

for $k = \{k_1, k_2\}$ with k_i integers. Above, $\Omega_0 = (0,1)^2$ is the unit square, and $\bar{v}$ denotes the complex conjugate of v. As before, we use the augmented Lagrangian formulation to write

$$\beta_k = \min_{v \in \mathcal{A}_k, F \in L^2(\Omega_0)} \max_{\Lambda \in L^2(\Omega_0)} \int_{\Omega_0} \left(\frac{1}{2} F \cdot \mathbb{L} F + \Lambda \cdot (\nabla v - F) + \frac{\rho}{2} |\nabla v - F|^2 \right) dx. \tag{29}$$

Recalling that v is a Bloch wave, and setting $F(x) = G(x)exp(i\omega_k \cdot x)$, $\Lambda(x) = g(x)exp(i\omega_k \cdot x)$, where $G, g \in L^2(\Omega_0)$ extended periodically, it follows that

$$\beta_k = \min_{p \in \mathcal{P}, G \in L^(\Omega_0)} \max_{g \in L^(\Omega_0)} \int_{\Omega_0} \left(\frac{1}{2} G \cdot \mathbb{L} G + g \cdot ((i\omega_k + \nabla)p - G) + \frac{\rho}{2} |(i\omega_k + \nabla)p - G|^2 \right) dx \tag{30}$$

where $\mathcal{P} = \{p \in H^1(\Omega_0) : ||p||_{L^2(\Omega_0)} = 1, p\ 1-\text{periodic}\}$. This saddle point problem can be solved as before using ADMM. Given G_i, p_i, g_i,

- *Step 1': Local problem.* Update G: $G_i = (\mathbb{L} + \rho\mathbb{I})^{-1}(g_i + \rho(i\omega_k + \nabla)p^n)$;
- *Step 2': Global update.* Update p: $(i\omega_k + \nabla)^2 p_{i+1} = (i\omega_k + \nabla) \cdot (G_{i+1} - \rho^{-1} g_i)$;
- *Step 3': Update Lagrange multiplier.* Update g: $g_{i+1} = g_i + \rho((i\omega_k + \nabla)p_{i+1} - G_{i+1})$;
- *Step 4': Check for convergence.*

Note that the global problem can be solved trivially in Fourier space.

Thus, a quadratic functional can be minimized over Bloch waves in the original unit cell with a slight modification of our algorithm.

3 GPU implementation

We begin with a brief introduction to general purpose GPUs and their use in computing, referring the reader to [30] for details. A compute node typically consists of a single CPU and one or more general purpose GPUs. While the clock speed of a CPU is faster than that of the GPU, the presence of thousands of cores and the architecture enables faster overall performance if properly organized. A schematic representation of a general purpose GPU is shown in Figure 1. It consists of a global or device memory and a number of streaming multiprocessors (SMs). Each SM in turn contains a number of cores or processors that have access to a shared memory, various registers and an instruction unit. All SMs also have access to the constant cache and the texture cache. The calculation is organized in threads with each processor typically executing a single thread. The threads are organized into warps. All threads in the warp work following the "single instruction multiple data

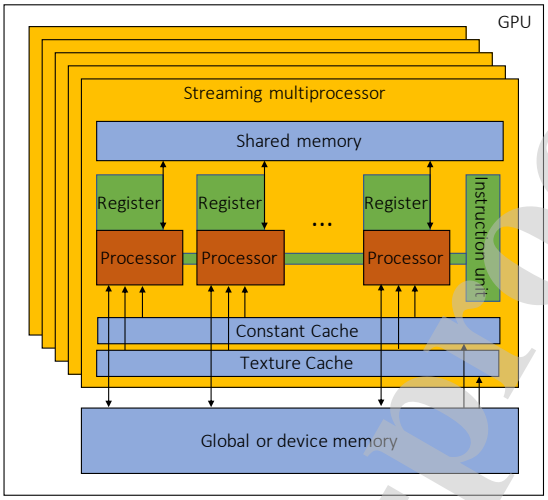

Figure 1: A schematic representation of the architecture of a general purpose graphical processing unit (adapted from [52])

(SIMD)" organization, i.e. each processor executes the same instruction concurrently with possibly different data. If there are many conditional instructions and different threads fall into different conditions, then it leads to a situation described as 'warp divergence' where each of the conditional instructions is executed in a serial manner. It is important to avoid warp divergence.

The exchange of data between a CPU and a GPU is slow, and therefore has to be minimized. Even though significantly faster, the exchange of data within a GPU between the global memory and the shared memory of a SM is also slow. However, this can be made faster using a parallel transfer strategy called 'coalesced memory access' [65] when a one to one mapping can be created between a thread and a segment of the global memory.

The implementation of the algorithm described earlier is presented in Algorithm 1. We work on a compute node consisting of a 14-core Intel Broadwell CPU and four Nvidia Tesla P100 GPUs. Each GPU contains 16GB of (global or device) memory and 56 SMs with 64 cores each for a total of 3584 cores, and has a double precision performance of 4.7 teraFLOPS. The P100 GPUs enable the compute unified device architecture (CUDA) platform with the standard programming language C++. CUDA uses warps of 32 threads [30]. The implementation is general and can be expanded to other platforms.

The algorithm takes advantage of the GPU architecture in various ways:

- All calculations are performed on the GPU. The CPU is used only for kernel function calls (i.e., to provide instructions to the GPU), initialization and output of results.
- The exchange of data between CPU and GPU is limited to the first initialization and to write results.
- Following first initialization, all data is kept on the GPU global memory during the entire calculation. Since the proposed algorithm uses the result of the previous time

Algorithm 1: Implementation on GPUs

Given an initial value of u^0, F^0, η^0 and macroscopic strain path $\overline{F}(t)$;
Step 0: Initialize:
  Place $\rho, \epsilon_p, \epsilon_d, \gamma_p, \gamma_d, f$ in constant cache;
  Place $u^0, F^0, \eta^0, \Lambda^0$ in global memory,
while $t < t_{max}$ **do**
  Initialize $F_0 = F^n, \eta_0 = \eta^n, u_0 = u^n, \Lambda_0 = \Lambda^n$
  while $r_p > \epsilon_p$ *or* $r_d > \epsilon_d$ **do**
    Step 1: Local problem.
    while $r_l > f r_d$ **do**
      Using kernel function:
        · Move $F_i, u_i, \eta_i, \Lambda_i$ to shared memory;
        · Fixed number of iterations to solve (14), (15) for F_{i+1}, η_{i+1};
        · Move F_{i+1}, η_{i+1} to global memory
      Compute r_l ; `/* cuBlas */`
    end
    Step 2: Helmholtz projection.
      · FFT $\widehat{F}_{i+1}$, $\widehat{\eta}_{i+1}$; `/* cuFFT */`
      · Using kernel function:
        · Move $\widehat{F}_{i+1}$, $\widehat{\eta}_{i+1}$ to shared memory;
        · Find $\widehat{u}_{i+1}$ from (23);
        · Move $\widehat{u}_{i+1}$ to global memory;
      · iFFT $\widehat{u}_{i+1}$; `/* cuFFT */`
    Step 3: Update Lagrange multiplier. Find Λ_{i+1} from (17) ; `/* cuBlas */`
    Step 4: Check for convergence Compute r_p, r_d from (18) ; `/* cuBlas */`
  end
  Update t, $F^{n+1}, u^{n+1}, \eta^{n+1}, \Lambda^{n+1}$
end

`cuBlas` and `cuFFT` are built-in CUDA kernal functions used in the indicated steps.

step to initialize the current time step, it is not necessary to perform any GPU/CPU transfer between time steps when there is no need to write the result.

- Global constants like the penalty and tolerance parameters are kept in constant cache.
- The local step 1 of the proposed algorithm is well-suited for SIMD since the same equations are solved independently at each point. Further, the structure enables optimization of the exchange between global and shared memory within the GPU in two ways. The data can be kept in shared memory within the SM during the local iterations. Therefore, the exchange between global and shared memory is limited to the initialization and to the final output of the local iteration. Even these transfers can exploit the coalesced memory access since each thread (point) only requires data stored at a particular location in global memory.

- The Helmholtz projection is local in Fourier space (cf. (23)). Therefore is it well-suited for SIMD, and can take advantage of coalesced memory access.
- The local nature of the local step 1 in real space and the Helmholtz projection in Fourier space avoid warp divergence.
- The computation of the L^2 norms in the approximate solution of step 1, the Lagrange multiplier update (step 3), the convergence check (step 4) are executed using basic linear algebra operations.
- Library functions that are optimized for GPUs are available for fast Fourier transform and basic linear algebra operations.

4 Bifurcation in finite elasticity

We start with a problem of finite deformation that involves a bifurcation, and one that has been previously studied using both computation in two dimensions [56, 9] and experiment [49, 9]. It serves as verification of the proposed method against previous results of Triantafyllidis, Nesterović and Schraad [56], Section 4.1. We also use this example to discuss convergence and scaling in Section 4.2.

4.1 Bifurcation

Consider a periodic arrangement of compliant circular inclusions in a stiff matrix in two dimensions as shown in Figure 2(a). Both materials are modeled as compressible Mooney-Rivlin materials with stored energy density

$$W(F,x) = \frac{\mu(x)}{2}(I_1 - \ln I_2 - 2) + \frac{\kappa(x)}{2}(\sqrt{I_2} - 1)^2 \tag{31}$$

where μ is the shear modulus and κ is the bulk modulus, and I_1 and I_2 are the first and second invariants of right Cauchy-Green tensor C. The moduli take the values μ_i, κ_i and μ_m, κ_m in the inclusion and the matrix respectively with $\mu_i < \mu_m, \kappa_i < \kappa_m$. In our numerical examples, $\kappa_i/\mu_i = \kappa_i/\mu_m = 9.8$ while $\mu_m/\mu_i = 20$.

We start with a 1×1 unit cell simulation. The periodic medium is subjected to equi-biaxial compression, $\langle F \rangle = \lambda I$ where λ decreases monotonically from an initial value of 1. At each given value of λ, the equilibrium solution is computed using Algorithm 1 on a 1024×1024 grid starting with the solution of the previous λ as an initial guess. We obtain the stress-stretch curve shown by square symbols (blue) in Figure 2(b) and a periodic solution with the deformed unit cell shown in Figure 2(c).

It is known that this example develops a long-wavelength instability. Note that a 1-periodic function is also $k-$periodic for any $k = (k_1, k_2), k_i$ integers. Thus, we may have equilibrium solutions that are periodic on a $k_1 \times k_2$ super-cell. However, it is known from Geymonat, Müller and Triantafyllidis [23] that the 1-periodic solution is the stable solution

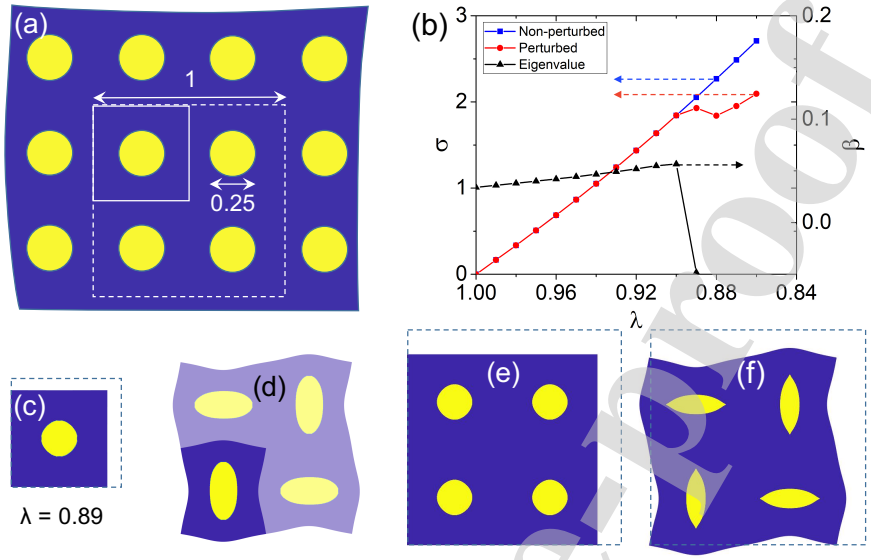

Figure 2: Bifurcation of a periodic composite. (a) A periodic composite with the unit cell (bold lines) and super cell (dashed line). (b) The stress-stretch curve without bifurcation (blue, square symbols) and with bifurcation (red, round symbols) along with the modulus of stability $\beta_{(2,2)}$ (black, triangle symbols). (c) Deformed shape of the unit cell (dashed line showing the undeformed size) at $\lambda = 0.89$. (d) The mode shape of the unstable mode in the period-doubling instability at $\lambda = 0.89$. (e) The deformed shape of the supercell without bifurcation at $\lambda = 0.89$. (f) The deformed shape of the supercell post bifurcation at $\lambda = 0.89$.

near $\lambda = 1$. However, this solution may become unstable as λ changes. By the second variation condition, the 1-periodic solution u remains stable as long as

$$\int_{\Omega_k} \nabla v \cdot \frac{\partial W^2}{\partial F \partial F}(\nabla u(x), x) \nabla v dx \geq 0 \tag{32}$$

for all non-zero $k-$periodic functions v. Using Bloch waves, this is equivalent to requiring $\beta_k \geq 0$ where β_k is as defined in (27).

Therefore, we compute the modulus of stability β_k for various k, and this is also shown with triangular symbols (black) in Figure 2(b). We see that $\beta_{(2,2)} \to 0$ as $\lambda \to 0.9$. The corresponding mode v_k is shown in Figure 2(d) as the darkened region. This suggests that the periodic solution will bifurcate to a solution that is periodic on a 2×2 super-cell.

We therefore repeat the finite deformation equilibrium computation on a 2×2 super-cell and a 2048×2048 mesh, once without a perturbation (i.e., with the solution to the previous λ as an initial guess), and once with the linearly unstable mode added as a perturbation (i.e., with the sum of the solution to the previous λ and a scaled eigenmode v_k associated with β_k as the initial guess). The simulation without a perturbation leads to a periodic solution as before Figure 2(e) and with the same stress-stretch curve shown in black in Figure 2(b). The perturbed solution also agrees with it until $\lambda \approx 0.9$, but then bifurcates into a solution

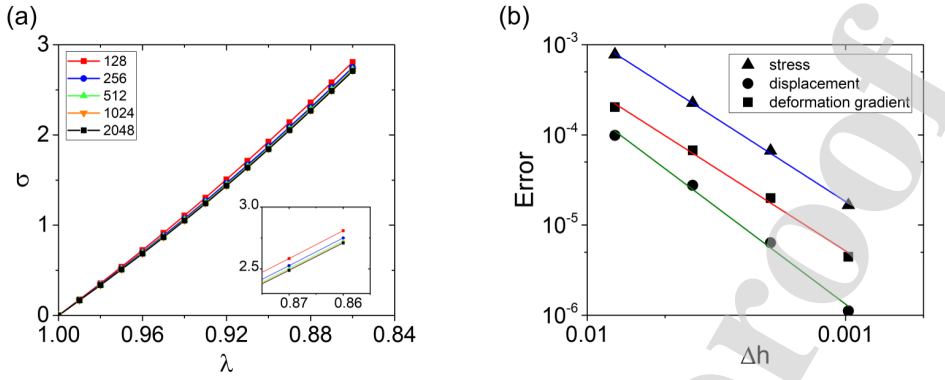

Figure 3: Convergence with mesh size. (a) Stress-stretch curve for various computational grid resolution and (b) Relative error in the deformation gradient and stress vs. grid size.

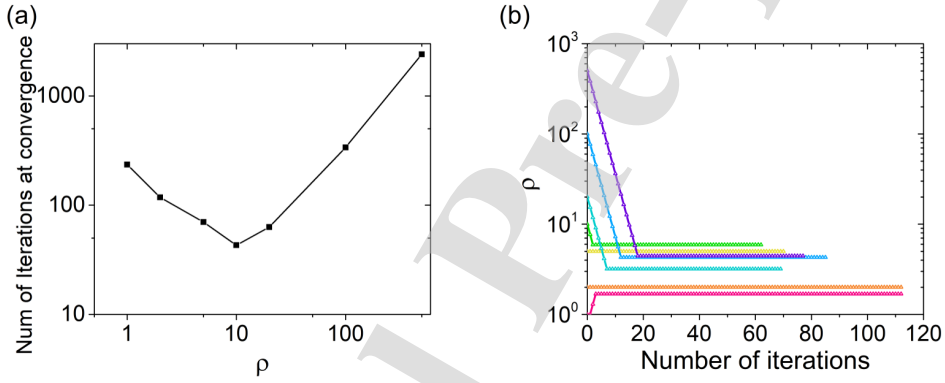

Figure 4: Effect of penalization parameter ρ on convergence. (a) Total number of iterations with different fixed ρ and (b)Variation of ρ starting from different values.

with period 2×2 shown in Figure 2(f) with a stress-stretch curve shown with round symbols (red).

All results agree with those of Triantafyllidis, Nesterović and Schraad [56], thereby verifying the method.

4.2 Convergence and performance

We now use this example to demonstrate convergence and scaling of the proposed algorithm. In all the tests, we compress the composite until $\lambda = 0.95$.

We begin by investigating the convergence with resolution. The simulation is performed with 128×128, 256×256, 512×512, 1024×1024, and 2048×2048 grids, and the stress-stretch curves are shown in Figure 3(a). Further, taking the 2048×2048 grid as the reference, Figure 3(b) shows how the relative error (L_2 norm) of deformation gradient and stress depend on resolution. We observe polynomial convergence with rates of 1.83 and 1.84 for the error in

deformation gradient and displacement respectively. These are very close to the expected rate of 2 for the discrete differential operator of FFT. We believe that these are due to the change in residual spurious oscillation at the interface as well as the change in pixellated geometric representation with resolution.

The effect of the penalization parameter ρ on the number of iterations required for a given error is shown in Figure 4. Figure 4(a) shows the number of iterations to achieve a given convergence (in primal and dual error) when ρ is held fixed at different values. We observe that the number of iterations increase for both small ρ and large ρ with the optimal at about $\rho = 10$. As noted earlier in Section 2.1, the primal error is large for small ρ and the dual error is large for large ρ. This is the reason that we adjust ρ following (20). We show the evolution of ρ for various initial values of ρ in Figure 4(b) with γ and τ in (20) set to 5 and 1.3 respectively. We note that in all cases, ρ converges exponentially to values from 3 to 10. Further, in contrast to the case with fixed ρ, the simulation converges well before 100 iterations. Thus, (20) ensures a robust convergence of ρ and significantly speeds up the algorithm. We have also observed in our numerical experiments that $\rho < 1$ leads to divergence early in the iteration.

We study the approximate solution of the local step 1 in Figure 5 using two strategies. The first strategy is to require convergence of the local iterations of Step 1 only on a fixed fraction of spatial points, and these results are shown in Figure 5(a,b). We check how many spatial points have converged to a given (pointwise) residual after a given number of local iterations and proceed to step 2 if a given percentage of spatial points have converged. This check requires a communication between the shared and device memory which adds time, but it can be expedited using coalesced memory (the time required for the memory transfer and check is comparable to the time required for a single local iteration in our examples). Figure 5(a,b,c) shows the results when the local residual is held to 10^{-11}, a check is performed every two local iterations and the percentage of converged points varied from 10% to 90%. We see from Figure 5(a) that the wall clock time for the global iteration to converge decreases monotonically with the percentage of converged points. Further, the number of global iterations necessary for global convergence is largely independent of the number of converged points. In other words, the approximate solution of the local step 1 has relatively little adverse effect on the global convergence. Indeed, we see from Figure 5(b) that the global dual residual decreases in the same manner as the calculations proceed, except each global iteration is faster thereby reducing the overall clock time.

The second strategy is to require that the local residual r_l be a fixed fraction of the global dual residual r_d, and the results are shown in Figure 5(c,d). We observe from Figure 5(c) that the wall clock time for global convergence decreases while the total number of global iterations necessary for global convergence remains unchanged as we increase the ratio r_l/r_d. In fact, at around a ratio of 0.3, we only require one or two iterations in the local step after a few global steps. Again, we see from Figure 5(d) that the global dual residual decreases in the same manner independent of the ratio r_l/r_d as the calculations proceed, except each global iteration is faster with increasing r_l/r_d thereby reducing the overall clock time.

Finally, we have verified that the error in the final solution obtained by either of these approximate approaches to local step 1 is negligible when compared to the solution obtained by the exact solution of step 1 (difference in the deformation gradient is comparable to machine error).

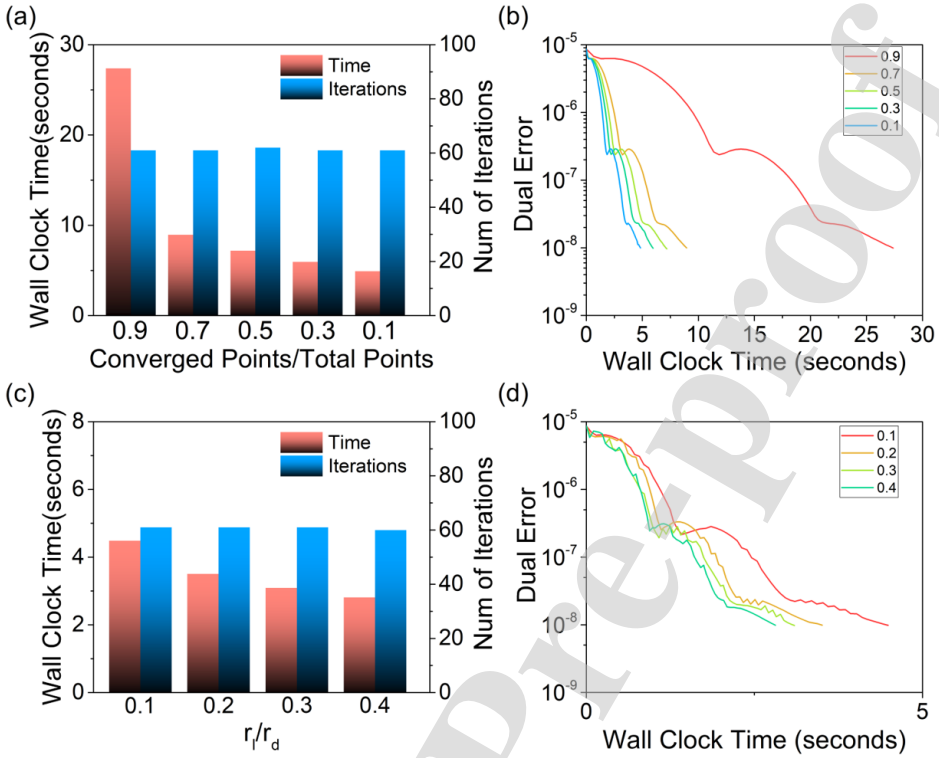

Figure 5: Performance with approximate solution of the local problem. (a,b) Local convergence on a fixed fraction of spatial points: (a) Wall clock time and number of global iterations for global convergence for various fractions. (b) The global dual error versus wall clock time for various fractions. (c,d) Fixed ratio of local (r_l) to global dual (r_d) residual: (c) Wall clock time and number of global iterations for global convergence for various ratios and (d) The global dual error versus wall clock time for various ratios.

These results show that approximate solution of the local step 1 is an effective strategy to improving performance of our method. In effect, we allow for larger tolerance in the local step when the global residual is large and exploit these in future iterations. Further, recall from Section 2.1 that the error in satisfying the (physical) equilibrium equation is bounded by the local and residual global error. In particular, the vanishing dual error implies vanishing local error as required by the Eckstein-Bertsekas condition [20]. Therefore, requiring the local residual to be a fraction of the global residual ensures physically meaningful solutions. Therefore, we adopt this strategy. Finally, we remark that this strategy is especially useful in highly nonlinear problems. The analogous results for our example in liquid crystal elastomers are shown in Figure 14 of the Appendix.

Finally, the parallel performance of the algorithm is examined in Figure 6. The problem with a 1024×1024 mesh is simulated with 128, 512, 2048, 8192 threads. We observe a steady decrease of wall time with increased threads of GPU. The slope is -0.73, suggesting a good scalability of the algorithm. We attribute the deviation from the perfect slope of -1

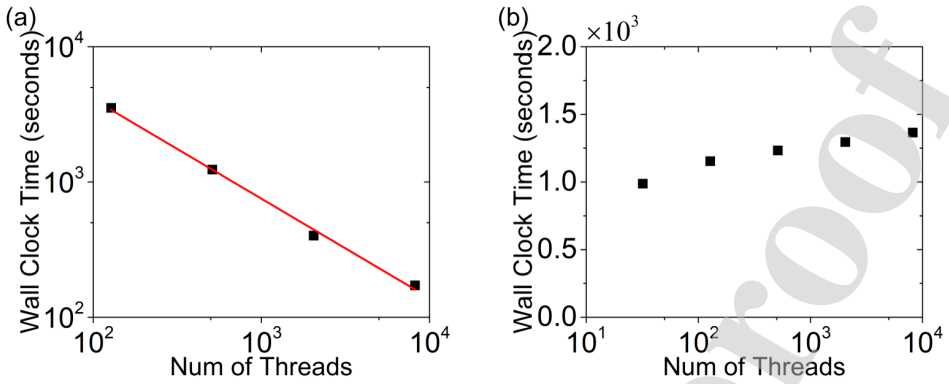

Figure 6: Parallel performance of the algorithm. (a) Strong scaling and (b) Weak scaling.

to two reasons. First, we use FFT which scales as $O(n \log n)$ with system size, and second, operations such as sum and norm also takes communication and do not scale linearly with the number of nodes. We note that the scaling improves for nonlinear problems as the local step 1 takes a larger fraction of the time. The analogous result for liquid crystal elastomers is shown in Figure 15 of the Appendix and the slope is -0.80. The scaling efficiency is confirmed by weak scaling. The same configuration is studied with a 128×128 grid using 32 threads, a 256×256 grid using 128 threads, a 512×512 grid using 512 threads, a 1024×1024 grid using 2048 threads, and a 2048×2048 grid using 8192 threads. Overall, the algorithm and GPU implementation show good parallel efficiency with system size.

5 Microstructure evolution in liquid crystal elastomers

We now apply the approach described and verified above to microstructure evolution in LCEs.

5.1 Liquid crystal elastomer formulation

We take the configuration in the isotropic state to be the reference configuration, but consider the material at a temperature below the phase transition temperature so that it is in the nematic phase. The state of the material at a material point x is then described by the deformation gradient $F(x)$, and a nematic director $n(x)$ that describes the orientation of the nematic mesogens in an infinitesimal volume around x. The material is typically incompressible and so $\det F = 1$, and n is a unit vector ($|n| = 1$) since it describes an orientation.

The free energy per unit volume of the material is given by,

$$W(F, n, \nabla n, x) = W_{el}(F, n) + W_{ni}(F, n, x) + W_F(\nabla n) \tag{33}$$

where the three terms describe three different physics. The first term,

$$W_{el}(F, n) = \frac{1}{2}\mu Tr(F^T \ell^{-1} F) \quad \text{where} \quad \ell = r^{-1/3}(\delta - (r-1)n \otimes n) \tag{34}$$

describes the entropic elasticity of the polymer network [14]. μ is the shear modulus, $\delta = Id$ is identity tensor, $r > 1$ represents the degree of nematic order that depends on temperature, and $\otimes$ represents the tensor product. We take r to be fixed since we fix temperature. Note that if $r = 1$, then $\ell = \delta$ and W_{el} reduces to the neo-Hookean energy [4]. For $r > 1$, the set of ground states ($W_{el} = 0$) corresponds to $F = R\ell_0^{1/2}Q, n = Re$ for rotations R, Q and fixed unit vector e. In other words, the material elongates along the director by factor $r^{1/3}$ and contracts perpendicular to it by factor $r^{-1/6}$, and the director is free to take any orientation. The second term,

$$W_{ni}(F, n, x) = \frac{1}{2}\mu\alpha Tr((\delta - n_0(x) \otimes n_0(x))F^T(n \otimes n)F) \tag{35}$$

describes the 'non-ideality' originating from non-uniformity in the cross-link density [12]. α is the strength of the non-ideality and $n_0(x)$ is a fixed random unit vector field. The non-uniformity in the cross-link density seeks to orient the director n parallel to Fn_0 at x, but this is a weak preference since α is typically small. Finally, the third term

$$W_F(\nabla n) = K|\nabla n|^2 = \frac{1}{2}K|\nabla(n \otimes n)|^2 \tag{36}$$

is (a constant coefficient approximation of) Frank elasticity [63, 64]. It reflects the preference of the directors to align spatially. It is easy to verify that both forms of the expression shown are equivalent using the fact that $|n| = 1$. We note for later use that $\sqrt{K/\mu}$ determines a length-scale of the domain wall and is typically $\mathcal{O}(10\text{nm})$ [63].

The evolution is controlled by a dissipation potential which we take to be

$$D(\dot{F}, \dot{n}) = \frac{1}{2}\nu_F|\dot{F}|^2 + \frac{1}{2}\nu_n|\dot{n}|^2 \tag{37}$$

Note that this expression is not frame-indifferent and there are a number of generalizations [41]. However, this is commonly used when the boundary conditions do not involve large rigid body rotations. The implicit time discretization of the evolution equation gives rise to the following variation problem (cf. 11)

$$u^{k+1}, n^{k+1} = \underset{|n|=1, \det \nabla u = 1}{\arg\min} \int_\Omega \left(W(\nabla u, n, \nabla n, x) + \Delta t D\left(\frac{\nabla u - \nabla u^k}{\Delta t}, \frac{n - n^k}{\Delta t} \right) \right) dx \tag{38}$$

Since ∇u and n satisfy constraints, one should consider the non-Euclidian metrics along the constraint manifold instead of the Euclidian metric in the embedding space. However, the approximate expressions are accurate to first order since the manifolds are smooth with curvature bounded from below.

We discretize space using finite differences and solve the resulting equations according to the massively parallel approach described in Sections 2 and 3 with two modifications. First, the constraint of incompressibility, $\det F = 1$, is enforced in the local Step 1 using a Lagrange multiplier; while the constraint on the director, $|n| = 1$ is enforced by introducing Euler angles. Second, we also have a gradient of $(n \otimes n)$ in our functional. We could proceed by introducing an auxiliary variable for $\nabla(n \otimes n)$ and using a constraint for it. However, we have found that we obtain satisfactory results by treating this term explicitly. All simulations are performed under periodic boundary conditions on the deformation gradient and the director.

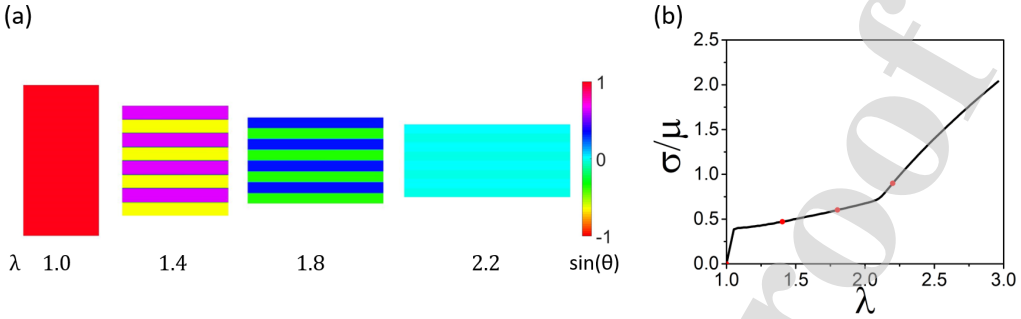

Figure 7: Two-dimensional study of a monodomain LCE subjected to uniaxial stress. (a) Evolution of the director (θ is the angle between the director and the horizontal loading direction). (b) Stress-stretch curve (stress is normalized by the modulus μ).

5.2 Monodomain LCE

We begin by studying a simple problem in two dimensions inspired by the experiments of Küpfer and Finkelmann [34]. We start with a monodomain specimen where $n_0 = e_2$ is uniformly in the vertical direction as shown in Figure 7. We normalize the energy density with μ and take the rest of the parameters to be $r = 4$, $\alpha = 0.1$, $K/\mu = 7.63 \times 10^{-6}$ (in non-dimensional length units). We set dissipation to zero taking $\nu_n = \nu_F = 0$ so that we solve for equilibrium at each time step. Finally, we subject the specimen to an average deformation gradient $\langle F_{11} \rangle = \lambda, \langle F_{12} \rangle = \langle F_{21} \rangle = 0$ and $\langle F_{22} \rangle$ free and solve it with a resolution of 256×256. We use the previous configuration along with a small periodic perturbation of the order 10^{-4} in F as the initial guess at each time step. The resulting domain patterns are shown in Figure 7(a) while the stress-stretch curve is shown in Figure 7(b). We observe the semi-soft behavior and stripe domains consistent with the experimental observations. The director is initially aligned with n_0 and there is no stress. At small applied stretch, the LCE reacts elastically as the non-ideal term keeps the director n aligned with n_0. At a critical stretch, the director can align, but doing so leads to a shear inconsistent with the imposed condition on the deformation gradient. Therefore, it forms stripe domains where the director rotates in opposite directions in alternating stripes; the two regions have the same stretch but opposing shear so that they can satisfy the imposed average deformation gradient condition. The spacing depends on the perturbation and κ. The formation of stripe domains is accompanied by a softening in the stress-stretch curve. The director continues to rotate as the stretching continues until it is fully rotated to the horizontal when both domains merge (since the sign of the director has no meaning). The stress-stretch curve then stiffens as the material responds elastically. All of this is consistent with the observations of Küpfer and Finkelmann [34] and prior theoretical considerations [63].

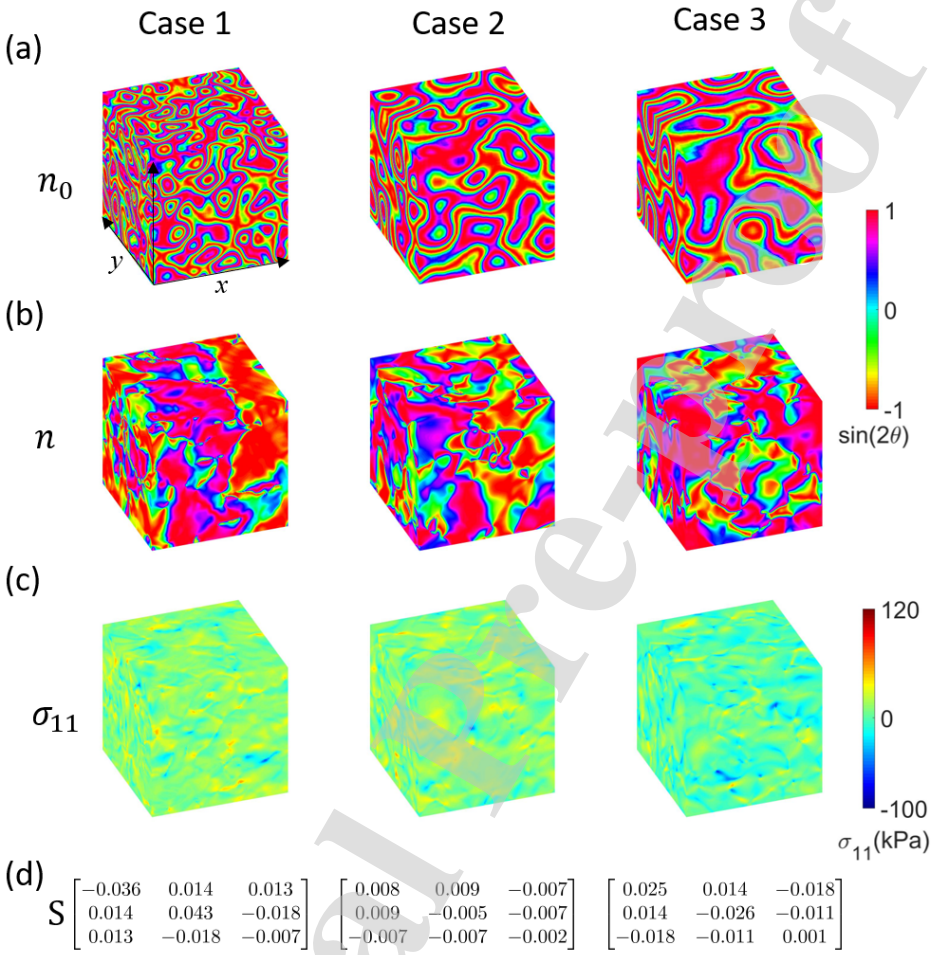

Figure 8: Creating the initial polydomain material. (a) Distribution of the preferred director n_0 with fluctuations on three length-scales, (b) Distribution of director n after relaxation, (c) Internal stress distribution and (d) Orientation parameters (below (39)) after relaxation. θ is the in-plane angle of mesogens w.r.t. $x-$axis.

5.3 Polydomain LCE

In this section, the parameters are $r = 7.71$, $\mu = 23.63$ kPa, $\alpha = 0.06$, $K = 3.61 \times 10^{-9}$N, $\nu_F = 2.65$ kPa.s and $\nu_n = 0.005$ kPa.s unless otherwise specified. These parameters are chosen to match the experimental results of Tokumoto *et al.* [55] as will be described later. We conduct our simulations on a $(1\ \mu\text{m})^3$ cubic unit cell with a 128^3 resolution at a strain rate of $1\ \text{s}^{-1}$ with time steps of 0.02s.

Polydomain material We begin by exploring the effect of the random director field n_0 on the initial configuration. Figure 8(a) shows three 'random' director fields n_0 with fluctuations

on a different length-scale. All three of them are generated by starting with the same Gaussian random field of angles and then filtering to different length scales. With an initial guess of $n = n_0, F = I$, we let the system relax under zero average stress and we obtain the director field n shown in Figure 8(b). We see that the relaxed n does not follow n_0, and the system is internally stressed as shown in Figure 8(c). Interestingly, the length-scale on which n fluctuates is similar in each of the three cases. It is larger than the length-scale of n_0 fluctuation in the first two cases, but similar in the third.

Importantly, n remains largely equi-distributed. We recall the definition of the orientation tensor [63]

$$S = Q\left(\langle n \otimes n - \frac{1}{3} I\rangle\right) \tag{39}$$

where $\langle\cdot\rangle$ denotes the average over the computational domain and $Q = (r-1)/(r+2)$ is a material parameter ($r = 7.71$ and so that $Q = 0.69$ in our computations). Note that S is a trace-free matrix whose eigenvalues are bounded by $2Q/3$ and -$Q/3$. The *mean orientational order parameter* S_m is the largest eigenvalue of S while the *biaxial order parameter* X is the difference between the two smallest eigenvalues of S. It follows that $Sm = 0, X = 0$ for equidistributed domains, $S_m = 2Q/3$ (= 0.46 in our calculations), $X = 0$ for perfectly aligned domains where n is uniform, $S_m = Q/6$ (= 0.115 in our calculations), $X = Q/2$ (= 0.345 in our calculations) for equidistributed domains in the plane. Figure 8(d) shows $S_m \approx 0, X \approx 0$ and n is essentially equi-distributed.

We may understand this initial relaxation as follows. Recall that the non-ideal term prefers that the director n follow the prescribed n_0 and the elastic energy prefers an elongation along director. However, this resulting distortion field may not be compatible leading to elastic energy. Further, the Frank energy penalizes the fluctuations in the director field. Thus, the competition among these three terms drives the relaxation, and the resulting director pattern is a compromise among them.

To verify this, we start with a 'compatible' initial director field n_0 that takes two distinct values $n_0^{\pm} = \{\pm 0.42, 0.91, 0\}$ in alternating stripes as shown in Figure 9(a,c). It is easy to verify that the two corresponding spontaneous stretches $(\ell(n_0^{\pm}))^{1/2}$ are kinematically compatible across an interface with normal e_2, i.e., we can find a rotation Q and a vector a such that $Q(\ell(n_0^+))^{1/2} - Q(\ell(n_0^-))^{1/2} = a \otimes e_2$. Thus, the director field $n = n_0$ and deformation with gradient $F = (\ell(n))^{1/2}$ is admissible and minimizes the sum of the first two terms in the energy (33). Thus we expect the solution to follow $n = n_0, F = (\ell(n))^{1/2}$ except close to the interface where we expect a transition layer with thickness of the order $\sqrt{K/\mu}$. We study five cases with distinct length-scales. As before, we start with $n = n_0, F = I$, and let the system relax under zero average stress. We obtain the director field n shown in Figure 9(b,c). If the length-scale is is sufficiently large (the first four cases), then n follows n_0 except near the interface where we see a transition layer as we expect. At smaller length-scales the Frank elasticity prevents n from completely relaxing to n_0; in other words the interfaces dominate. This calculation shows that kinematic compatibility drives the relaxation with the Frank elasticity setting the length-scale.

Uniaxial and biaxial deformation These simulations are motivated by the experiments reported in Tokumoto *et al.* [55]. They took $65 \times 65 \times 0.7$ mm sheets and subjected them to

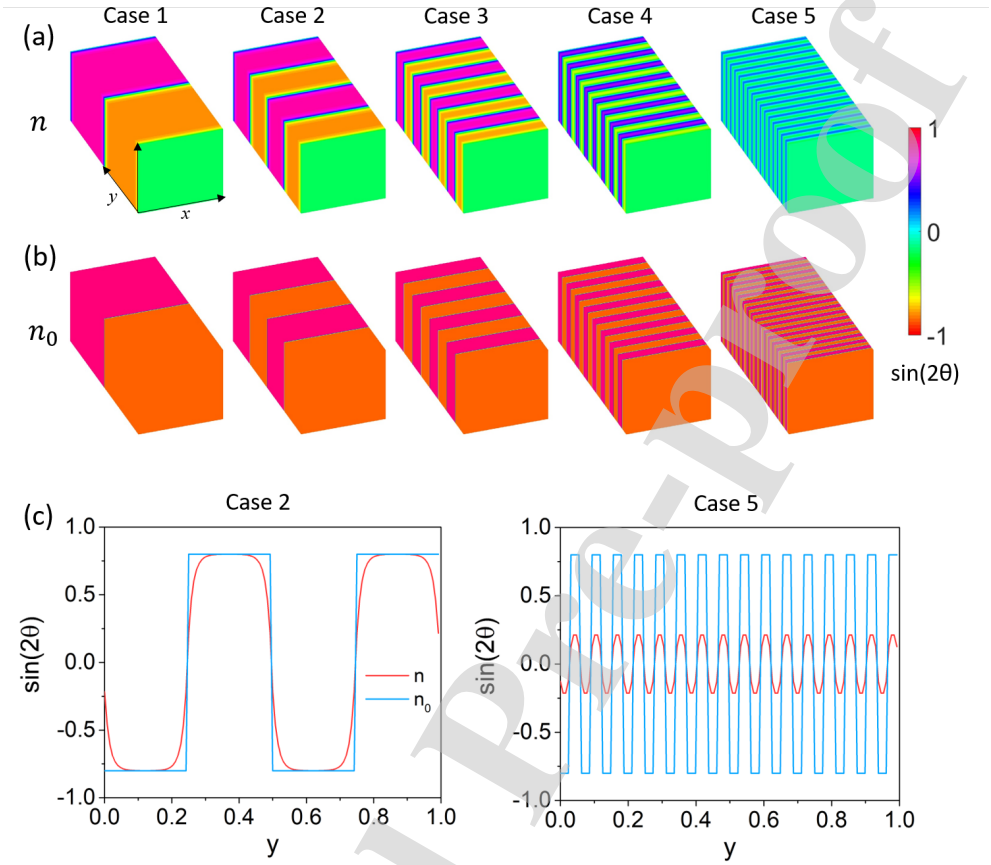

Figure 9: Relaxation of a stripe polydomain. (a) Distribution of the compatible preferred director n_0 with multiple length-scales, (b) Distribution of director n after relaxation (θ is the in-plane angle of mesogens w.r.t. $x-$axis and $\sin 2\theta$ is the product of the x and y components of the director.). (c,d) Details of the director field: the y-component of the director versus the y-coordinate for the second (c) and last cases (d) of (a,b).

uniaxial stress and biaxial stretch protocols. To replicate these experiments, we start with a relaxed polydomain specimen prepared as described above and subject it to three loading protocols.

- UNI: uniaxial stress ($\langle F_{11}\rangle$ is prescribed while all other components are free);
- PE: uniaxial stretch of a sheet in plane stress ($\langle F_{11}\rangle = \lambda_x, \langle F_{12}\rangle = 0, \langle F_{22}\rangle = 1$ while the other components are free);
- EB: equi-biaxial extension of a sheet in plane stress ($\langle F_{11}\rangle = \langle F_{22}\rangle = \lambda_x, \langle F_{12}\rangle = 0$ while the other components are free).

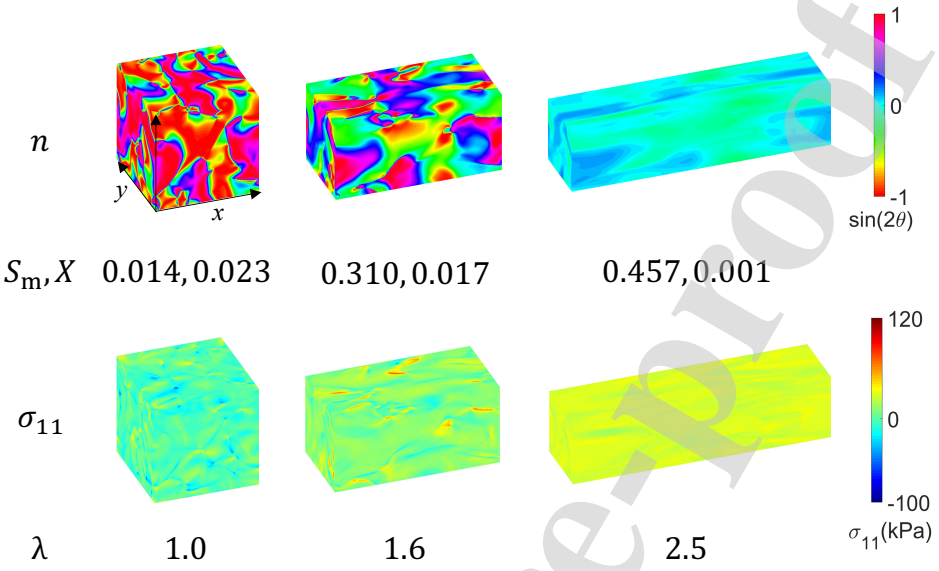

Figure 10: Uniaxial stress (UNI). Evolution of the director, the orientation parameters (below (39)) and the stress with stretch.

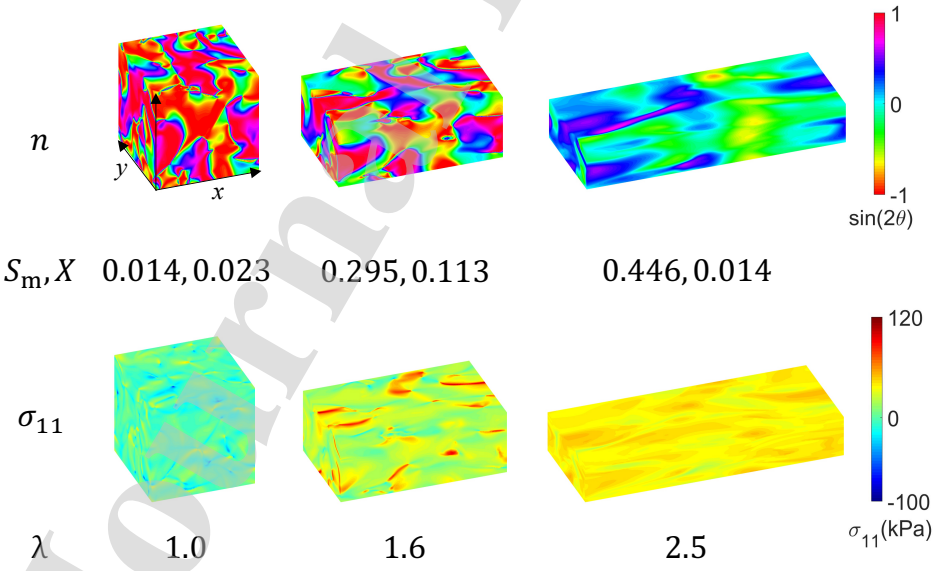

Figure 11: Uniaxial stretch of a sheet in plane stress (PE). Evolution of the director, the orientation parameters (below (39)) and the stress with stretch.

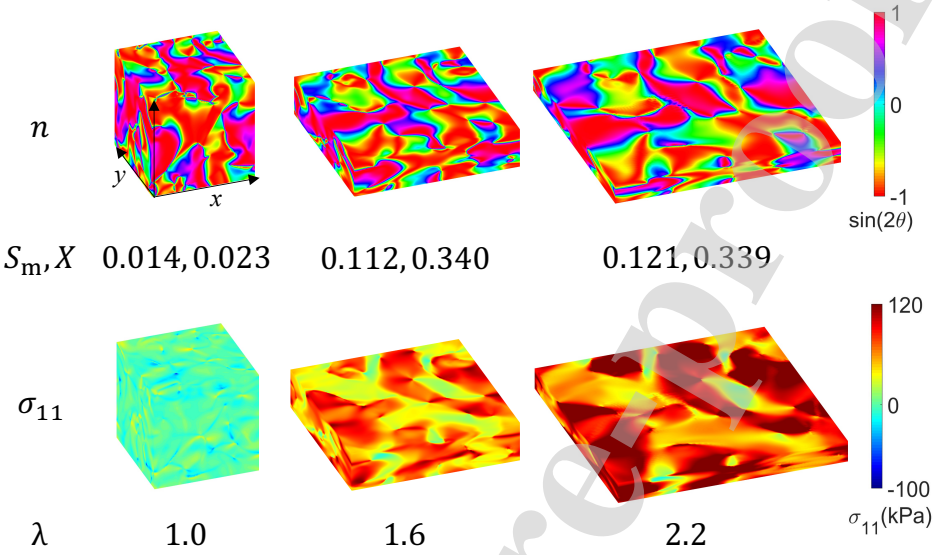

Figure 12: Equi-biaxial stretch of a sheet in plane stress (EB). Evolution of the director, the orientation parameters (below (39)) and the stress with stretch.

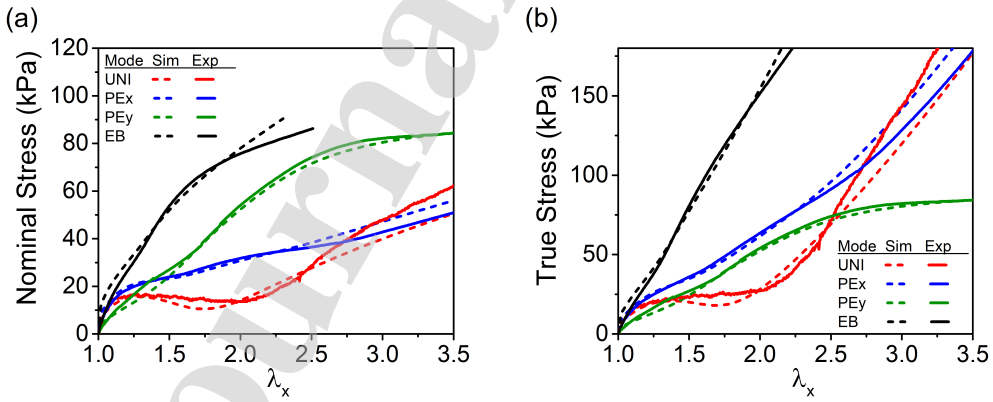

Figure 13: Stress vs. stretch for various loading protocols (UNI, PE and EB) obtained by both simulation (dashed line) and experiment (solid line). (a) Nominal stress vs. stretch and (b) True stress vs. stretch.

Note that PE and EB are mixed boundary conditions on the unit cell. Since $\langle F_{i3} \rangle$ and $\langle F_{3i} \rangle$ are left free and part of the minimization, the average tractions on the faces with normal e_3 are zero, and the average tractions on the other faces are planar. This corresponds to plane stress. At the same time, the average planar stretch is prescribed. The evolution of the director and the stress are shown in Figures 10, 11 and 12. The macroscopic stress-strain curve is shown in Figure 13 and compared to experimental observations.

We observe that the director pattern, residual stress and overall stress-strain curve are very different in the different loading scenarios. In uniaxial stress (UNI, Figure 10), the directors rotate until they all eventually align. This is similar to the situation in the ideal material (Figure 7) though the actual patterns are more complicated. Any residual fluctuations are small and this is also reflected in the small stress heterogeneity. This microstructure evolution leads to a soft plateau in the macroscopic stress-strain response which eventually stiffens when all the directors are aligned.

In the case of uniaxial stretch in plane stress (PE, Figure 11), the directors again try to rotate to the direction of elongation, but are prevented from doing so by the lateral constraint. Therefore, significant amounts of residual microstructure and some residual stress persist. Further, the macroscopic stress-strain response shows only a small plateau. The macroscopic stress-strain response also shows another rather interesting feature. The nominal stress and thus the applied force in the stretching (x) direction is smaller than those in the constrained (y) direction. This is counter-intuitive, and different from the behavior of ordinary elastomers. The reason for it is evident by examining the true or Cauchy stress: we observe the true stresses are (almost) equal in the two directions despite the fact that the stretches in the two directions. In other words, we are in a state of equi-biaxial stress with no shear stress. Cesana *et al.* [17] predicted a region of equi-biaxial stress in ideal materials ($\alpha = K = 0$). This behavior remains in non-ideal materials.

In the case of equi-biaxial stretch (EB, Figure 12), the directors orient gradually to become planar, but there is little, if any, evolution beyond that. There is also consequently significant heterogeneity in the state of stress. Together, the three results show that shear of unequal stretch drives microstructure evolution.

Finally, we compare our simulations with the experimental observations of Tokumoto *et al.* [55]. To do so, we pick values for ν_n and K consistent with prior work. We then fit the remaining four parameters (r, μ, α, ν_F) to the experimental (nominal) stress-stretch relationship for UNI and PE using least squares (i.e., minimizing the L_2 norm). These lead to the values reported at the beginning of the section. The comparison between the experimental and simulated stress-stretch relations is shown in Figure 13. We see the fit as well as the agreement in EB (which is not used in the fit) is excellent. This is remarkable because all simulations are carried out with only six parameters.

6 Conclusion

We have presented an approach to solving problems of computational micromechanics that is amenable to massively parallel calculations through the use of graphical processing units and other accelerators. The approach is based on splitting the solution operator in a manner that exploits the structure of continuum models that combine linear and universal physical

laws (kinematic compatibility, balance laws), and nonlinear but local constitutive relations. We verify the approach against previous numerical simulations and study convergence and performance using finite elasticity. We then study microstructure evolution in polydomain liquid crystal elastomers. Our results are in agreement with recent experimental observations, and in fact provides new insights into polydomain states and the mechanisms responsible for some counter-intuitive properties under multiaxial loading.

We conclude with a discussion of extensions and open issues. We use the Gaussian approximation to describe the elasticity of the polymer network in (33). This is known to be a poor approximation at very large stretches and one can generalize this [1]. Similarly, we use very simple models of dissipation and these can be generalized [66]. However, these also require more experimental to characterize. More ambitiously, it will be useful to develop macroscopic continuum models by combining the insights from the computational results presented here. This is current work in progress.

Turning now to the computational approach, we note that the method can be applied to a variety of problems. These include crystal plasticity, martensitic phase transformations, twinning, precipitation and Landau-Ginzburg models since these problems lead to equations of the form (1,2). Further, the implementation and examples presented here concern periodic boundary conditions which enabled the use of fast Fourier transforms to solve Poisson's equation. However, periodic boundary conditions are not inherent to this approach. The key issue is the solution of Poisson's equation, and there are a number of parallel iterative approaches that have been implemented with accelerators [60]. The problem of liquid crystal elastomers showed that we can incorporate point-wise constraints (incompressibility and prescribed norm on a vector internal variable) naturally in this method. It is possible to extend this approach to problems like fracture and contact where one has inequality constraints. Finally, one can extend this method to phenomena that include higher derivatives by introducing additional auxilliary variables. An important open question is the convergence of the algorithm and error estimates. We have noted in Section 2.1 that there are partial results in the case of convexity. However, the general case where W is quasi-convex in F and convex in the internal variables remains open. Further, systematic analysis of the error remains a topic for the future.

Appendix

Equilibrium condition We show that the dual feasibility ensures satisfaction of the equilibrium equation of mechanics. We begin with the case when the local problem (step 1) is solved exactly. Consider a smooth test function $\varphi : \Omega \to \mathbb{R}^3$ that vanishes on the boundary. Multiply (16) with φ, integrate over the domain and use the divergence theorem to obtain

$$\int_\Omega \nabla\varphi \cdot \left(\rho(F^{n+1} - \nabla u^{n+1}) - \Lambda^n\right) dx = 0. \tag{40}$$

Now multiply (14) with $\nabla\varphi$ and integrate over the domain to obtain

$$\int_\Omega \nabla\varphi \cdot \left(W_F(F^{n+1}, \eta^{n+1}, x) - \Lambda^n + \rho(\nabla u^n - F^{n+1})\right) dx = 0. \tag{41}$$

Subtract one from the other and we obtain

$$\int_\Omega \nabla\varphi \cdot W_F(F^{n+1}, \eta^{n+1}, x) dx = \rho \int_\Omega \nabla\varphi \cdot (\nabla u^{n+1} - \nabla u^n) dx. \tag{42}$$

By the dual feasibility $(18)_2$ and the Cauchy-Schwarz inequality, the right hand side above goes to zero. Further, the left hand side converges to the weak from of the equilibrium equation since this holds for arbitrary φ.

When the local step is not exact, we rewrite (40)

$$\begin{aligned}&\int_\Omega \nabla\varphi \cdot W_F(F^{n+1}, \eta^{n+1}, x) dx = \\ &\rho \int_\Omega \nabla\varphi \cdot (\nabla u^{n+1} - \nabla u^n) dx + \int_\Omega \nabla\varphi \cdot \left(W_F(F^{n+1}, \eta^{n+1}, x) - \Lambda^n + \rho(\nabla u^n - F^{n+1})\right) dx.\end{aligned} \tag{43}$$

The first term on the right is bounded by dual feasibility $(18)_2$ and the Cauchy-Schwarz inequality as before, and the second term is bounded by the local error estimate and the Cauchy-Schwarz inequality. Thus the weak form of the equilibrium equation holds.

Convergence and performance in the case of LCEs Figure 14 shows the performance of the algorithm when we have an approximate solution of the local problem (step 1). As in the case of the elasticity problem discussed in Section 4.2, we find that the approximate solution provides savings in time without affecting the overall global convergence.

Figure 15 shows the strong scaling in the case of liquid crystal elastomers. The slope is -0.80, which is in fact better than that observed in the case of elasticity. This is because the local step 1 which scales linearly takes a larger fraction of time compared to the case of elasticity. We have not performed the analysis of weak scaling since the specification of n_0 typically depends on the spatial resolution and therefore one-to-one comparison between simulations with different resolutions is not possible.

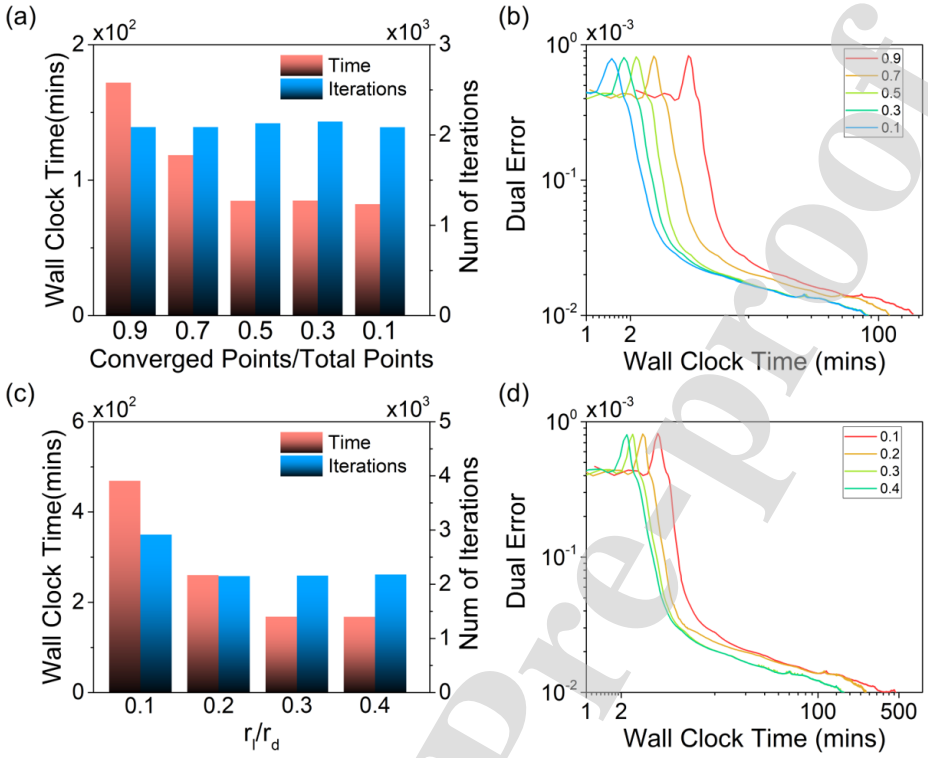

Figure 14: Performance with an approimate solution of the local problem in the case of liquid elastomers. (a,b) Local convergence on a fixed fraction of spatial points: (a) Wall clock time and number of global iterations for global convergence for various fractions. (b) The global dual error versus wall clock time for various fractions. (c,d) Fixed ratio of local (r_l) to global dual (r_d) residual: (c) Wall clock time and number of global iterations for global convergence for various ratios and (d) The global dual error versus wall clock time for various ratios.

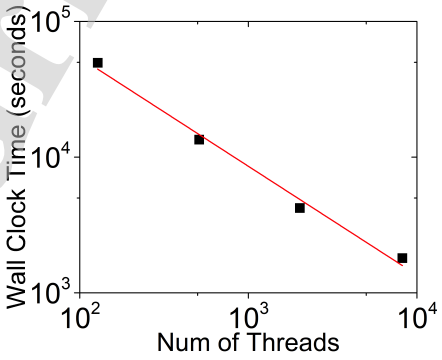

Figure 15: Strong scaling in the case of liquid crystal elastomers.

Acknowledgement

We are delighted to acknowledge many stimulating discussions with Pierre Suquet (concerning FFT algorithms) and Kenji Urayama (concerning LCEs). The latter also generously provided us with experimental data shown in Figure 13. We gratefully acknowledge the support of the US Air Force Office for Scientific Research through the MURI grant number MURI grant FA9550-16-1-0566. The computations presented here were performed at the High Performance Computing Center of California Institute of Technology.

References

[1] V. Agostiniani and A. Desimone. Ogden-type energies for nematic elastomers. *International Journal of Non-Linear Mechanics*, 47:402–412, 2012.

[2] B. Anglin, R. Lebensohn, and A. Rollett. Validation of a numerical method based on fast Fourier transforms for heterogeneous thermoelastic materials by comparison with analytical solutions. *Computational Materials Science*, 87:209–217, 2014.

[3] A. Artemev, Y. Jin, and A. Khachaturyan. Three-dimensional phase field model of proper martensitic transformation. *Acta Materialia*, 49(7):1165–1177, 2001.

[4] R. J. Atkin and N. Fox. *An introduction to the theory of elasticity*. Longman, 1980.

[5] A. Azoug, V. Vasconcellos, J. Dooling, M. Saed, C. Yakacki, and T. Nguyen. Viscoelasticity of the polydomain-monodomain transition in main-chain liquid crystal elastomers. *Polymer*, 98:165–171, 2016.

[6] S. Berbenni, V. Taupin, K. S. Djaka, and C. Fressengeas. A numerical spectral approach for solving elasto-static field dislocation and g-disclination mechanics. *International Journal of Solids and Structures*, 51:4157–4175, 2014.

[7] S. Berbenni, V. Taupin, and R. A. Lebensohn. A fast Fourier transform-based mesoscale field dislocation mechanics study of grain size effects and reversible plasticity in polycrystals. *Journal of the Mechanics and Physics of Solids*, 135:103808, 2020.

[8] N. Bertin and L. Capolungo. A FFT-based formulation for discrete dislocation dynamics in heterogeneous media. *Journal of Computational Physics*, 355:366–384, 2018.

[9] K. Bertoldi, M. C. Boyce, S. Deschanel, S. Prange, and T. Mullin. Mechanics of deformation-triggered pattern transformations and superelastic behavior in periodic elastomeric structures. *Journal of the Mechanics and Physics of Solids*, 56:2642–2668, 2008.

[10] K. Bhattacharya and P. Suquet. A model problem concerning recoverable strains of shape-memory polycrystals. *Proceedings of the Royal Society A: Mathematical, Physical and Engineering Sciences*, 461:2797–2816, 2005.

[11] J. Biggins, M. Warner, and K. Bhattacharya. Elasticity of polydomain liquid crystal elastomers. *Journal of the Mechanics and Physics of Solids*, 60(4):573–590, 2012.

[12] J. S. Biggins, E. M. Terentjev, and M. Warner. Semisoft response of nematic elastomers to complex deformations. *Physical Review E*, 78:041704, 2008.

[13] J. S. Biggins, M. Warner, and K. Bhattacharya. Supersoft elasticity in polydomain nematic elastomers. *Physical Review Letters*, 103(3):037802, 2009.

[14] P. Bladon, E. M. Terentjev, and M. Warner. Transitions and instabilities in liquid crystal elastomers. *Physical Review E*, 47:R3838, 1993.

[15] B. Bourdin, G. A. Francfort, and J.-J. Marigo. The variational approach to fracture. *Journal of Elasticity*, 91:5–148, 2008.

[16] S. Boyd, N. Parikh, E. Chu, B. Peleato, J. Eckstein, et al. Distributed optimization and statistical learning via the alternating direction method of multipliers. *Foundations and Trends in Machine learning*, 3:1–122, 2011.

[17] P. Cesana, P. Plucinsky, and K. Bhattacharya. Effective behavior of nematic elastomer membranes. *Archive for Rational Mechanics and Analysis*, 218:863–905, 2015.

[18] S. Conti, A. DeSimone, and G. Dolzmann. Soft elastic response of stretched sheets of nematic elastomers: a numerical study. *Journal of the Mechanics and Physics of Solids*, 50:1431–1451, 2002.

[19] A. DeSimone and G. Dolzmann. Macroscopic response of nematic elastomers via relaxation of a class of so (3)-invariant energies. *Archive for Rational Mechanics and Analysis*, 161(3):181–204, 2002.

[20] J. Eckstein and D. P. Bertsekas. On the Douglas-Rachford splitting method and the proximal point algorithm for maximal monotone operators. *Mathematical Programming*, 55:293–318, 1992.

[21] A. Eghtesad, M. Zecevic, R. A. Lebensohn, R. J. McCabe, and M. Knezevic. Spectral database constitutive representation within a spectral micromechanical solver for computationally efficient polycrystal plasticity modelling. *Computational Mechanics*, 61:89–104, 2018.

[22] D. J. Eyre and G. W. Milton. A fast numerical scheme for computing the response of composites using grid refinement. *The European Physical Journal-Applied Physics*, 6:41–47, 1999.

[23] G. Geymonat, S. Müller, and N. Triantafyllidis. Homogenization of nonlinearly elastic materials, microscopic bifurcation and macroscopic loss of rank-one convexity. *Archive for Rational Mechanics and Analysis*, 122:231–290, 1993.

[24] R. Glowinski. *Variational Methods for the Numerical Solution of Nonlinear Elliptic Problems*. Society for Industrial and Applied Mathematics, Philadelphia, PA, 2015.

[25] R. Glowinski. ADMM and Non-convex Variational Problems. In Glowinski, R and Osher, SJ and Yin, W, editor, *Splitting Methods in Communication, Imaging, Science and Engineering*, Scientific Computation, pages 251–299. Springer, Cham, Switzerland, 2016.

[26] R. Glowinski and P. Le Tallec. Numerical solution of problems in incompressible finite elasticity by augmented Lagrangian methods. I. Two-dimensional and axisymmetric problems. *SIAM Journal on Applied Mathematics*, 42:400–429, 1982.

[27] R. Glowinski and P. Le Tallec. Numerical solution of problems in incompressible finite elasticity by augmented Lagrangian methods II. Three-dimensional problems. *SIAM Journal on Applied Mathematics*, 44:710–733, 1984.

[28] R. Glowinski and P. Le Tallec. *Augmented Lagrangian and operator-splitting methods in nonlinear mechanics*. SIAM, Philadelphia, 1989.

[29] B. He, H. Yang, and S. Wang. Alternating direction method with self-adaptive penalty parameters for monotone variational inequalities. *Journal of Optimization Theory and Applications*, 106:337–356, 2000.

[30] D. B. Kirk and W.-M. W. Hwu. *Programming Massively Parallel Processors*. Morgan-Kaufman, 2016.

[31] M. Knezevic and D. J. Savage. A high-performance computational framework for fast crystal plasticity simulations. *Computational Materials Science*, 83:101–106, 2014.

[32] D. Kothe, S. Lee, and I. Qualters. Exascale Computing in the United States. *Computing in Science and Engineering*, 21:17–29, 2019.

[33] I. Kundler and H. Finkelmann. Strain-induced director reorientation in nematic liquid single crystal elastomers. *Macromolecular Rapid Communications*, 16(9):679–686, 1995.

[34] J. Küpfer and H. Finkelmann. Nematic liquid single crystal elastomers. *Die Makromolekulare Chemie, Rapid Communications*, 12:717–726, 1991.

[35] R. A. Lebensohn, A. K. Kanjarla, and P. Eisenlohr. An elasto-viscoplastic formulation based on fast Fourier transforms for the prediction of micromechanical fields in polycrystalline materials. *International Journal of Plasticity*, 32:59–69, 2012.

[36] R. A. Lebensohn and A. Needleman. Numerical implementation of non-local polycrystal plasticity using fast Fourier transforms. *Journal of the Mechanics and Physics of Solids*, 97:333–351, 2016.

[37] S. Lucarini and J. Segurado. An algorithm for stress and mixed control in Galerkin-based FFT homogenization. *International Journal for Numerical Methods in Engineering*, 119:797–805, 2019.

[38] B. L. Mbanga, F. Ye, J. V. Selinger, and R. L. Selinger. Modeling elastic instabilities in nematic elastomers. *Physical Review E*, 82(5):051701, 2010.

[39] J. Michel, H. Moulinec, and P. Suquet. A computational method based on augmented Lagrangians and fast Fourier transforms for composites with high contrast. *Computer Modelling in Engineering and Sciences*, 1:79–88, 2000.

[40] A. Mielke. A mathematical framework for generalized standard materials in the rate-independent case. In R. Helmig, A. Mielke, and B. K. Wohlmuth, editors, *Multifield Problems in Solid and Fluid Mechanics*, pages 399–428. Springer, 2006.

[41] A. Mielke, C. Ortner, and Y. Şengül. An approach to nonlinear viscoelasticity via metric gradient flows. *SIAM Journal on Mathematical Analysis*, 46:1317–1347, 2014.

[42] B. Mihaila, M. Knezevic, and A. Cardenas. Three orders of magnitude improved efficiency with high-performance spectral crystal plasticity on gpu platforms. *International Journal for Numerical Methods in Engineering*, 97:785–798, 2014.

[43] G. W. Milton. Substitution of subspace collections with nonorthogonal subspaces to accelerate Fast Fourier Transform methods applied to conducting composites. arXiv Preprint: 2001.08289, 2020.

[44] N. Mishra, J. Vondřejc, and J. Zeman. A comparative study on low-memory iterative solvers for FFT-based homogenization of periodic media. *Journal of Computational Physics*, 321:151–168, 2016.

[45] V. Monchiet and G. Bonnet. A polarization-based FFT iterative scheme for computing the effective properties of elastic composites with arbitrary contrast. *International Journal for Numerical Methods in Engineering*, 89:1419–1436, 2012.

[46] H. Moulinec and F. Silva. Comparison of three accelerated FFT-based schemes for computing the mechanical response of composite materials. *International Journal for Numerical Methods in Engineering*, 97:960–985, 2014.

[47] H. Moulinec and P. Suquet. A fast numerical method for computing the linear and nonlinear mechanical properties of composites. *Comptes Rendus de l'Académie des Sciences Paris*, 318:1417–1423, 1994.

[48] H. Moulinec, P. Suquet, and G. Milton. Convergence of iterative methods based on Neumann series for composite materials: Theory and practice. *International Journal for Numerical Methods in Engineering*, 114:1103–1130, 2018.

[49] T. Mullin, S. Deschanel, K. Bertoldi, and M. C. Boyce. Pattern transformation triggered by deformation. *Physical Review Letters*, 99:084301, 2007.

[50] M. Ortiz and L. Stainier. The variational formulation of viscoplastic constitutive updates. *Computer Methods in Applied Mechanics and Engineering*, 171:419–444, 1999.

[51] P. Plucinsky and K. Bhattacharya. Microstructure-enabled control of wrinkling in nematic elastomer sheets. *Journal of the Mechanics and Physics of Solids*, 102:125–150, 2017.

[52] T. Preis, P. Virnau, W. Paul, and J. J. Schneider. GPU accelerated Monte Carlo simulation of the 2D and 3D Ising model. *Journal of Computational Physics*, 228:4468–4477, 2009.

[53] J. R. Rice. Inelastic constitutive relations for solids: An internal-variable theory and its application to metal plasticity. *Journal of the Mechanics and Physics of Solids*, 19:433–455, 1971.

[54] M. Schneider. An FFT-based method for computing weighted minimal surfaces in microstructures with applications to the computational homogenization of brittle fracture. *International Journal for Numerical Methods in Engineering*, 121:1367–1387, 2020.

[55] H. Tokumoto, H. Zhou, A. Takebe, K. Kamitani, A. Koijo, A. Takahara, K. Bhattacharya, and K. Urayama. Probing the in-plane liquid-like behavior of liquid crystal elastomers. *submitted*, 2020.

[56] N. Triantafyllidis, M. Nestorović, and M. Schraad. Failure surfaces for finitely strained two-phase periodic solids under general in-plane loading. *Journal of Applied Mechanics*, 73:505–515, 2006.

[57] N. Uchida. Elastic effects in disordered nematic networks. *Physical Review E*, 60(1):R13, 1999.

[58] N. Uchida. Soft and nonsoft structural transitions in disordered nematic networks. *Physical Review E*, 62(4):5119, 2000.

[59] K. Urayama, E. Kohmon, M. Kojima, and T. Takigawa. Polydomain- monodomain transition of randomly disordered nematic elastomers with different cross-linking histories. *Macromolecules*, 42(12):4084–4089, 2009.

[60] W. van Rees, D. Rossinelli, P. Hadjidoukas, and P. Koumoutsakos. High performance CPU/GPU multiresolution Poisson solver. *Advances in Parallel Computing*, 25:481–490, 01 2014.

[61] A. Vidyasagar, W. Tan, and D. M. Kochmann. Predicting the effective response of bulk polycrystalline ferroelectric ceramics via improved spectral phase field methods. *Journal of the Mechanics and Physics of Solids*, 106:133–151, 2017.

[62] J. Vondřejc, J. Zeman, and I. Marek. An FFT-based Galerkin method for homogenization of periodic media. *Computers & Mathematics with Applications*, 68:156–173, 2014.

[63] M. Warner and E. M. Terentjev. *Liquid crystal elastomers*. Oxford University Press, Oxford, 2003.

[64] P. J. Wojtowicz, P. Sheng, and E. Priestley. *Introduction to liquid crystals*. Springer, 1975.

[65] B. Wu, Z. Zhao, E. Z. Zhang, Y. Jiang, and X. Shen. Complexity analysis and algorithm design for reorganizing data to minimize non-coalesced memory accesses on GPU. *ACM SIGPLAN Notices*, 48:57–68, 2013.

[66] Y. Zhang, C. Xuan, Y. Jiang, and Y. Huo. Continuum mechanical modeling of liquid crystal elastomers as dissipative ordered solids. *Journal of the Mechanics and Physics of Solids*, 126:285–303, 2019.

[67] H. Zhou, R. Lebensohn, P. Reischig, W. Ludwig, and K. Bhattacharya. Imposing equilibrium on measured 3-D stress fields using Helmholtz decomposition and FFT-based optimization. *In preparation*, 2020.

[68] T. Zohdi and P. Wriggers. *Introduction to computational micromechanics*. Springer Verlag, 2005.

Declaration of interests

☒ The authors declare that they have no known competing financial interests or personal relationships that could have appeared to influence the work reported in this paper.

☐The authors declare the following financial interests/personal relationships which may be considered as potential competing interests: